Mixing and crystal scavenging in the Main Ethiopian Rift revealed by trace element systematics in feldspars and glasses

Fiona Iddon[1]*, Charlotte Jackson[1], William Hutchison[2], Karen Fontijn[3], David M. Pyle[3], Tamsin A. Mather[3], Gezahegn Yirgu[4] and Marie Edmonds[1]

[1] Department of Earth Sciences, University of Cambridge

[2] School of Earth and Environmental Sciences, University of St Andrews

[3] Department of Earth Sciences, University of Oxford

[4] School of Earth Sciences, Addis Ababa University

Corresponding author: Fiona Iddon (fei20@cam.ac.uk)

Key Points:

- Alkali feldspars have variable trace element (Ba) concentrations, some far from equilibrium with their carrier liquids (melts).
- Some feldspars are *antecrysts* (in equilibrium with a liquid on the line of descent, but not the host melt), picked up from a crystal mush.
- Ignimbrites erupted during caldera-forming events are dominated by antecrysts, perhaps scavenged from deep parts of the magma reservoir.

Abstract

For many magmatic systems, crystal compositions preserve a complex and protracted history which may be largely decoupled from their carrier melts. The crystal cargo may hold clues to the physical distribution of melt and crystals in a magma reservoir and how magmas are assembled prior to eruptions. Here we present a geochemical study of a suite of samples from three peralkaline volcanoes in the Main Ethiopian Rift. Whilst whole-rock data shows strong fractional crystallisation signatures, the trace element systematics of feldspars, and their relationship to their host glasses, reveals complexity. Alkali feldspars, particularly those erupted during caldera-forming episodes, have variable Ba concentrations, extending to high values that are not in equilibrium with the carrier liquids. Some of the feldspars are antecrysts, which we suggest are scavenged from a crystal-rich mush. The antecrysts crystallised from a Ba-enriched (more primitive) melt, before later entrainment into a Ba-depleted residual liquid. Crystal-melt segregation can occur on fast timescales in these magma reservoirs, owing to the low viscosity nature of peralkaline liquids. The separation of enough residual melt to feed a crystal-poor post-caldera rhyolitic eruption may take as little as months to tens of years (much shorter than typical repose periods of 300-400 years). Our observations are consistent with these magmatic systems spending significant portions of their life cycle dominated by crystalline mushes containing ephemeral, small (< 1 km^3) segregations of melt. This interpretation helps to reconcile observations of high crustal electrical resistivity beneath Aluto, despite seismicity and ground deformation consistent with a magma body.

Index Terms:

1036, 1065, 1042, 8428, 8145

Keywords:

Peralkaline, Main Ethiopian Rift, crystal mush, crystal scavenging, antecryst, magma mixing

1 Introduction

Studies of magma storage and migration in the crust over the past decade have challenged traditionally held views of magma chambers as large, molten melt bodies (see reviews by Cashman & Giordano, 2014; Cashman & Sparks, 2013; Cashman et al., 2017). High-precision, high-resolution geochemical studies of erupted volcanic products have revealed previously undetected complexities at the mineral scale. Many systems show evidence of magmas being stored, between eruptions, at near-solidus conditions for prolonged periods of time (e.g. Bachmann & Bergantz, 2008; Cashman et al., 2017; Cooper & Kent, 2014). Heterogeneous crystal cargoes in volcanic rocks, which are often not in equilibrium with their carrier liquids, suggest that mixing may be ubiquitous. Crystal-rich mushes may be disrupted and disaggregated prior to and during eruptions, leading to the accumulation of a range of diverse crystals in the magma; e.g. Fish Canyon Tuff (Bachmann et al., 2002), Shiveluch Volcano (Humphreys et al., 2008), Mount Hood (Cooper & Kent., 2014), and Yellowstone (Wotzlaw et al., 2014). Added to these geochemical lines of evidence, geophysical imaging of the upper crust has often failed to detect large bodies of melt beneath active volcanoes (e.g. Hübert et al., 2018; Manzella et al., 2004; Samrock et al., 2015). This has led to suggestions that, in some circumstances, magmas

may be stored as melt-poor mush, which is expected to have a low electrical conductivity and low V_p/V_s ratio (Chu et al., 2010; Miller & Smith, 1999; Steck et al., 1998; Zandt et al., 2003).

Many studies are published on the crystal cargoes of large magma reservoirs in metaluminous, calc-alkaline magmatic systems; to date, there has been little attention paid to the crystal cargoes of peralkaline magma reservoirs, despite their prevalence in continental rift settings. There are few constraints on the architecture and dynamics of peralkaline magma reservoirs, and little is known about the types of geophysical signals such magma bodies would generate. Peralkalinity, defined as having an excess of alkalis with respect to aluminium (molar $(Na_2O+K_2O)/Al_2O_3>1$; Shand et al., 1927), has a strong influence on melt rheology, and thus magma behaviour (Lanzo et al., 2013; Neave et al., 2012; Stevenson & Wilson, 1997). The elevated alkali content of peralkaline melts, coupled with high dissolved halogen contents (Barclay et al., 1996), results in peralkaline liquids having much lower viscosity (by 2 to 3 log units) compared to their metaluminous counterparts, particularly at temperatures approaching the solidus (di Genova et al., 2013). The low viscosity of peralkaline melts likely influences magma reservoir processes. Crystal-melt segregation via settling and/or compaction within the crustal storage system may occur faster than in metaluminous arc settings for similar melt SiO_2 contents (Macdonald, 2012; Neave et al., 2012), and magma reservoirs may become more rapidly density-stratified, hindering overturn and mixing (Blake & Ivey, 1986; Macdonald, 2012; Mahood & Hildreth, 1986; Neave et al., 2012; Peccerillo et al., 2003).

The Main Ethiopian Rift (MER) is a northerly segment of the East African Rift system (EARS) (**figure 1a**), a present-day example of continental rifting. Whole-rock compositions of rift magmas are commonly bimodal (Boccaletti et al., 1995; Gasparon et al., 1993; Hutchison et al., 2016c; Macdonald et al., 2011; Mazzarini et al., 2004; Peccerillo et al., 2003; Rooney et al., 2012; Ronga et al., 2010; Trua et al., 1999). Alkali basalts erupt outside the calderas and along faults (Mazzarini et al., 2013; Rooney et al., 2011), whilst peralkaline trachytes and rhyolites dominate the eruptive products from axis-central volcanoes. Isotope and trace element systematics of whole-rock material indicate the rhyolites are derived from protracted fractional crystallisation of an alkali basalt parent (Giordano et al., 2014; Hutchison et al., 2016c; Hutchison et al., 2018; Macdonald et al., 2011; Peccerillo et al., 2003). Modelling suggests that the least evolved trachytes at Gedemsa Volcano (location shown in **figure 1b**) are generated after ~70% fractional crystallisation of the basalts, and peralkaline rhyolite after an additional ~20% (Peccerillo et al., 2003). The transition to peralkalinity in these magmas occurs after 80 to 85% crystallisation, when the dominant crystallising phase changes from sodic plagioclase to alkali feldspar (Bailey & Schairer, 1964; Barberi et al., 1974), causing the melt to evolve towards the minimum in the Na_2O-K_2O-Al_2O_3-SiO_2 system (Carmichael & Mackenzie, 1963).

Despite seemingly simple whole-rock geochemical signatures, controlled by fractional crystallisation, there is petrological and geochemical evidence for more complex magma processing prior to eruptions at MER volcanic centres. For example, heterogeneous glass compositions, zoned feldspar and clinopyroxene phenocrysts, and resorbed feldspar and olivine phenocrysts have been cited as evidence for magma mixing at Boset-Bericha volcano (Macdonald et al., 2011), whilst mingled glass compositions have been observed at Chefe Donsa (Rooney et al., 2012) and intermediate-composition enclaves have been found in erupted products from Aluto (Hutchison et al., 2016c) (locations shown in **figure 1b**). High Ba and Mn concentrations in porphyritic trachytes from Gedemsa volcano (location shown in **figure 1b**) have been linked to feldspar and fayalite accumulation, with mass balance calculations

suggesting a minimum of 10% crystal accumulation (Peccerillo et al., 2003). The resorbed nature of some phenocrysts is consistent with an antecrystic nature (Peccerillo et al., 2003). The petrology of these complex erupted products may encode information about how magmas are stored and remobilised during eruptions, which may be relevant to interpreting geophysical data acquired in the region. Significant portions of melt may be held in crystal-rich magma reservoirs, ready to be remobilised and extracted (e.g. Bachmann & Bergantz, 2008; de Silva et al., 2008; Ruprecht & Bachmann, 2010; Wark et al., 2007), but these melt regions can be difficult to detect using geophysical techniques. For example, there is debate concerning the current state of the magma reservoir beneath Aluto volcano. Seismic and deformation data, combined with geobarometric estimates and Holocene eruptive frequency (Fontijn et al., 2018; Hutchison et al., 2016a; Hutchison et al., 2016c; Wilks et al., 2017), point to the existence of a shallow magma storage system. However, magnetotelluric methods fail to identify a volume of enhanced electrical conductivity in the crust (Hübert et al., 2018; Samrock et al., 2015) that might indicate the presence of partial melt (e.g. Pous et al., 1999; Hoffman-Rothe et al., 2011; Schilling & Partzsch, 2001). In contrast, enhanced electrical conductivity, interpreted as the presence of crustal melt, has been imaged in similar surveys at the nearby Boset-Bericha volcano (Whaler & Hautot, 2006).

We hypothesise that melt-poor mush may dominate magma reservoir storage systems beneath central volcanoes in the MER, and that this mush may be efficiently constructed in peralkaline magmatic systems due to their unique rheological characteristics. To test this hypothesis we undertake a systematic comparison between whole-rock, glass and feldspar compositions for a suite of samples from three peralkaline MER volcanoes, Aluto, Kone, and Fentale (locations shown in **figure 1b**). We focus on Ba, as it partitions strongly into alkali feldspars, the overwhelmingly dominant crystallising phase in evolved peralkaline magmas; and on Zr, a highly incompatible element in peralkaline melts and a useful proxy for fractional crystallisation. We evaluate the extent to which the crystal cargo is in equilibrium with its carrier liquid by comparing the results from the natural samples with experimental partitioning data for Ba using models of fractional crystallisation generated from RhyoliteMELTS (Gualda et al., 2012). Models of crystal settling and compaction (Bachmann & Bergantz, 2004) are used to assess the degree of influence of peralkaline liquid rheology on timescales of crystal-melt segregation processes. Finally, inferences about the types of geophysical signals such magma bodies would generate are made, helping to inform future volcanic monitoring activities along the MER.

2 Geological Setting

The MER is part of the EARS (**figure 1a**), a continental rift between the Nubian and Somalian plates (see reviews by Corti, 2009; Ebinger, 2005). Extending in a NNE-SSW direction from the Afar to the Turkana depression (Mohr, 1983; WoldeGabriel et al., 1990), the MER is currently undergoing active east-west extension of ~5 mm yr^{-1} (Saria et al., 2014). Extension was initially accommodated by displacement along NE-SW trending faults (Bonini et al., 2005; WoldeGabriel et al., 1990). Since 2 Ma, strain has largely been accommodated on the Wonji Fault Belt (WFB) (Corti, 2009) and recent geodetic data confirms that 80% of the current strain is accommodated on the WFB (Bilham et al., 1999). The WFB is a group of short N-NE trending en-echelon faults that lie within a ~15 km wide axial zone in the MER (Agostini et al., 2011; Keir et al., 2006; Keir et al., 2015). Pleistocene and Holocene volcanism has been focused within

tectono-magmatic segments along the rift that are co-located with the WFB (Abebe et al., 2007; Corti, 2009; Fontijn et al., 2018; Keir et al., 2006; Keir et al., 2015; Rooney et al., 2011).

Aluto, Kone, and Fentale are peralkaline caldera complexes located in the MER (**figure 1b and 1c, 1d, and 1e, respectively**). Whole-rock compositions, petrographic descriptions and geochronology for Aluto volcanic products are presented by Hutchison et al. (2016c), and for Fentale by Gibson (1974) and Giordano (2014). In contrast, there are few data available for Kone volcano. Cole (1968) and Rampey et al. (2010) provide descriptions of major map units, however previous petrographic and geochemical investigations have largely been limited to a Plinian eruptive deposit known as the Gubisa formation (**figure 1d**, Rampey et al., 2014), with some limited data also available on basalts that infill the caldera structure (Furman et al., 2006; Rooney et al., 2007; Rooney et al., 2012).

The Kone central volcanic complex comprises the older ~95 km^2 caldera (Birenti), and the younger, 22 km^2 Kone caldera with a small embayment of 2 km^2 known as the Korke caldera (Rampey et al., 2010, 2014) (**figure 1d**). Both structures are thought to have formed during a multi-eruption event, with the later Kone and Korke calderas developing during a series of 3-4 sub-Plinian and Plinian eruptions (Rampey et al., 2010, 2014). The Gubisa formation is associated with the formation of the Kone caldera (**figure 1d**); deposits are up to 60 m thick with a minimum volume of 3.2 km^3 (Rampey et al., 2014). Deposits associated with caldera-forming events are well preserved and dominate surface exposure at the Kone volcanic complex. Trachytic and rhyolitic lava domes and associated minor deposits of pumice preceded and followed the caldera-forming events. There are no dates available for Kone eruptions, though tectonically-controlled basaltic lava effusion, exploiting the join between the Kone and Korke calderas and filling both structures (**figure 1d**), likely represents the most recent volcanism (Fontijn et al. 2018; Rampey et al., 2010, 2014). Basaltic scoria cones and fissure lavas are also present to the Southwest and Northeast (**figure 1d**), aligned with the WFB (Rampey et al., 2010, 2014).

Fentale volcano is the northernmost silicic centre in the MER, located at the junction with the Afar region (**figure 1b**) (Gibson 1967, 1969, 1970, 1974). It is a 600 m high stratocone built of silicic lava flows and rare tephra horizons, with a 300 m deep summit caldera known as Tilik volcano (**figure 1e**) (Gibson 1967, 1969, 1970, 1974; Giordano et al., 2014; Kidane et al., 2009; Webster et al., 1993). The 30 km^2 caldera is roughly elliptical in shape and is thought to have formed during an explosive eruption between 0.17 and 0.151 Ma (Williams et al., 2004). The deposits of this eruption are widespread, forming intensely welded tuffs up to 30 m thick, blanketing the plain and covering the slopes of the earlier edifice (**figure 1e**) (Giordano et al., 2014). Post-caldera volcanism consists largely of obsidian lava flows from vents within the caldera itself and on the volcano's flanks, as well as from fissures along the rim (Acocella et al., 2002; Gibson 1967, 1969, 1970, 1974; Fontijn et al., 2018; Webster et al., 1993; Williams et al., 2004). Minor post-caldera explosive episodes have also occurred, with scattered pumice observed on the edifice slopes (Fontijn et al., 208) and a significant pumice cone on the southern flank. Similar to Kone, the most recent activity was mafic, primarily on the southwestern side of the volcano, where the WFB intersects the Fentale complex. Here fissure lavas cover a 3 km^2 area (**figure 1e**) and have been dated to ~ 1810-1820 based on oral tradition (Harris, 1844).

At Aluto volcano at least 8-21 km^3 of welded, green rhyolitic ignimbrites and trachytic tuffs erupted during the formation of a 42 km^2 caldera structure at ca. 300 ka. It is not possible to identify if this was a singular or multiple-eruption event, due to the generally poor surface

exposure of these deposits (Hutchison et al., 2015, 2016c). Post-caldera volcanism has been ongoing since at least ca. 60 ka, possibly after a significant hiatus (Hutchison et al., 2016c), and dominates the exposed volcanic rocks (**figure 1c**). These post-caldera eruptions are thought to typically initiate with explosive eruptions, building small pumice cones and/or emplacing pyroclastic density currents, before effusive eruptions of obsidian coulées (Hutchison et al., 2016c). Basaltic volcanism is largely confined to scoria cones and fissure lavas to the North-East of the main edifice (**figure 1c**). Hutchison et al. (2016c) suggest a relationship between the basalts and the caldera system based on proximity and comparable surface weathering of eruptive products, though the cones are strongly aligned with the WFB. It is hypothesised that silicic magma chambers in the MER act as mechanical density filters, forcing mafic melts to erupt externally to caldera margins (Peccerillo et al., 2003). The most recent dated eruption occurred several hundred years ago (0.4 ± 0.05 cal ka BP; Hutchison et al., 2016c), and at least 25 eruptions are identified in the Holocene period (Fontijn et al. 2018).

Episodes of ground deformation, thought to have a magmatic origin, have occurred at Aluto volcano over at least the past decade (Biggs et al., 2011; Hutchison et al., 2016a). InSAR observations show periods of rapid inflation followed by periods of long-term subsidence. The inflation is thought to reflect fluid injection into the roof zone of a magma storage region, whilst subsidence was interpreted as magmatic degassing and depressurisation of the hydrothermal system (Hutchison et al., 2016a). The deformation is consistent with a source at ~5 km depth. Seismicity has been identified between 2-9 km depth, which also reflects magmatic fluids causing elastic deformation (Wilks et al., 2017). However, magnetotelluric methods fail to identify a volume of enhanced electrical conductivity at this depth in the crust (Hübert et al., 2018; Samrock et al., 2015) that might indicate the presence of partial melt (e.g. Pous et al., 1999; Hoffman-Rothe et al., 2011; Schilling & Partzsch, 2001).

3. Analytical Techniques

The Aluto samples used in this study were collected by Will Hutchison between 2012 and 2014. The Kone samples were collected by both Michael Rampey between 2001 and 2003 and Karen Fontijn and Keri McNamara in November 2015. The Fentale samples were collected by Fiona Iddon, Jonathan Hunt, and Abate Assen in October 2017. Caldera-forming ignimbrites, post-caldera silicic lava and pumice, and later post-caldera basaltic lava and scoria were collected at each site. Where available pre-caldera silicic lava and pumice and pumice associated with caldera forming episodes was also utilised in the study. See **table 1 and 2** for all sample locations, refer to Hutchison et al. (2016c) for full details on the Aluto samples.

Kone and Fentale samples were trimmed to access clean regions and then crushed and milled to produce powders. X-ray fluorescence spectrometry (XRF) analysis was used to acquire whole-rock major and trace element compositional data on fusion beads and powder pellets respectively. Loss on ignition (LOI) was determined at 950 °C . Data was acquired at the Department of Geology at the University of Leicester using a PANalytical Axios-Advanced XRF spectrometer. Precision of 5% for majors (11% for MnO, 8% for P_2O_5) and 6% for trace elements was achieved using a range of secondary standards; Ba showed a precision of 4% and Zr a precision of 1%. An accuracy of 7% (11% for P_2O_5) was achieved for majors and 10% for trace elements; Ba was analysed with an accuracy of 9% and Zr an accuracy of 6%. Standards compilations can be found in **supplementary material**. Precision and accuracy (in %) were calculated as $100\ \frac{\sigma}{\bar{x}}$ and $100\ \frac{(\bar{x}-x_{ref})}{x_{ref}}$ respectively.

Polished sections (30-50 μm thick) were used for petrographic analysis and geochemical analyses of phenocryst phases. The Quanta-650F Scanning Electron Microscope (SEM) at the Department of Earth Sciences of the University of Cambridge was used to acquire back-scattered electron (BSE) images and maps to assess sample crystal fraction and to provide microtextural information. A 15 kV beam and 4 μm spot was used for Aluto samples; a 10 kV beam and 5 μm spot was used for Kone samples (images were acquired by different operators). QEMSCAN software was used for quantative analysis, and to assess the major phases present and major element zoning. The QEMSCAN software creates phase assemblage maps from data acquired from a combination of low-count energy-dispersive X-ray spectra (EDX) and BSE brightness and X-ray count information. Fiji software, an open source image processing package (Schindelin et al., 2012), was used to quantitatively assess crystal fraction.

Chemical compositions of the main phases and the matrix glass were measured using a Cameca SX-100 Electron Probe Micro-Analyser (EPMA) at the University of Cambridge. An accelerating voltage of 15 kV was used for all analysis. A defocused beam of 10 μm and a current of 10 nA was used for was used for glass analyses. A precision and accuracy of 6% for major elements (precision of 10% for MnO and 9% for P_2O_5; accuracy of 8% for MnO and 41% for P_2O_5) was achieved using a range of secondary standards. Plagioclase and alkali feldspar were also measured using a 10 nA beam but with a defocused beam of 5 μm. Pyroxenes were measured using a 1 μm sized beam with a current of 10 nA. For all phases some trace elements were measured using a second condition with a higher current voltage of between 40 and 100 nA. Counting times of 10-30 s were used for major elements, 40-90 s for trace elements and 10-12 s for alkalis. Where the beam current was increased to 100 nA, for example for the measurement of Ba and Sr within feldspars, counting times of up to 400 s were used. A precision of 6% and an accuracy of 3% for major elements (precision of 31% for TiO_2 and 16% for K_2O; accuracy of 19% for TiO_2 and 8% for K_2O) was achieved using a range of secondary standards. Standards compilations can be found in **supplementary material**.

Trace element analysis of matrix glasses was acquired by secondary ion mass spectrometry (SIMS) using a Cameca ims-4f ion probe at the School of Geosciences at the University of Edinburgh. Glass chips were hand-picked from crushed material and mounted in epoxy blocks, which were then gold-coated. A 25 mm square area was rastered with a low beam current prior to analysis, to remove the gold coating and any contamination. A range of standards was used to construct a robust calibration and analysed at the beginning and end of every session to assess data quality. Precision of 4% and accuracy of 7% was achieved for all trace elements; Ba was measured with a precision of 1% and an accuracy of 7%; Zr with a precision and accuracy of 2%. Standards compilations can be found in **supplementary material**.

4 Results

4.1 Petrographic descriptions

4.1.1 Alkali basalt

The alkali basalts are present as both porphyritic seriate lava and scoria (**figure 2a**). Phenocrysts are typically up to a few mm in size, and represent from 5.5 to 26 absolute volume % (vol%) of the scoria samples and up to 45 vol % of the lava samples. Phases include plagioclase, olivine and augite (modal proportions of the phenocrysts of 78%, 22% and 0% for the lavas, and 40%, 35% and 25% for the scoria). Glomerocrysts are common, at up to 4 mm

287 across they mainly comprise olivine and plagioclase, although clinopyroxene (**figure 2a**) is
288 particularly common in the scoria. Zoning is present in all phases (**figure 2a**), particularly
289 associated with the glomerocrysts. Olivine and plagioclase phenocrysts show normal zoning,
290 with rare occurrences of reverse-zoned olivine rims. Augite phenocrysts show oscillatory zoning.
291 Chrome spinels are generally present in the groundmass of both lavas and scoria, and as
292 inclusions within the phenocrysts.

293

294 4.1.2 Caldera-forming eruptions

295 Large-volume ignimbrite eruptions are associated with caldera-forming phases at Aluto,
296 Kone and Fentale (Fontijn et al., 2018; Gibson, 1967, 1970, 1974; Giordano et al., 2014;
297 Hutchison et al., 2016c; Rampey et al., 2010, 2014). Samples selected for study are all intensely
298 welded. Ignimbrite bulk compositions straddle the trachytic to rhyolitic boundary (**figure 3a**) and
299 are crystal-rich, with phenocrysts accounting for 17 to 35 absolute volume % (**figure 2b and 2c**).
300 The crystal population is dominated (up to 85 modal % proportion of the phenocrysts) by broken
301 euhedral feldspars up to 3 mm in size, which vary from oligoclase to anorthoclase to sanidine,
302 with the former more abundant in the less evolved samples, the latter in the most evolved (**figure**
303 **2b and 2c**). Some feldspars display normal zoning, with plagioclase cores (**figure 2b**);
304 occasional andesine (up to 5 modal %) is also present. Other phases include fayalite (up to 5
305 modal % in less evolved samples), with alteration rims, fractured quartz (up to 25 modal % in
306 more evolved samples), rounded or elongate aegirine-augite (up to 10 modal %) and aenigmatite
307 (up to 10 modal %). Most of these phases are up to 0.5 mm in size, but can reach up to 2.5 mm in
308 size in some cases. The phenocrysts can form a glomeroporphyritic texture, with clots up to 5
309 mm in size (**figure 2b and 2c**), set in a variably devitrified groundmass. Fe-Ti oxides are present
310 as microphenocrysts, 0.1-0.2 mm in size, clustering in and around the glomerocrysts (**figure 2b**).
311 Xenoliths of rhyolite and trachyte lava are common, particularly in rhyolitic ignimbrites, as are
312 finely crystalline fiamme and collapsed vesicles (**figure 2c**). The unwelded pumiceous fall
313 material, associated with caldera-forming eruptions, has a similar phase assemblage to the
314 rhyolitic ignimbrites and shows similar textures (**figure 2d**), although it has a lower phenocryst
315 content (<10 vol %).

316

317 4.1.3 Pre and post-caldera eruptions

318 Felsic lava and pumice is erupted during pre- and post-caldera phases. Samples selected
319 for study include pre-Birenti caldera, pre-Kone caldera and post-Kone caldera lava from Kone,
320 pre- and post-caldera lava from Fentale and post-caldera lava and pumice from Aluto. Trachytic
321 lava, and occasional rhyolite lava, contain up to ~30 vol % phenocrysts (**figure 2e**), dominated
322 by euhedral sanidines (>70 modal %) up to 3 mm in size, and small rounded quartz crystals (up
323 to 25 modal %) 0.2-0.3 mm in size. Aegirine-augite (<2.5 modal %) up to 2 mm in size, and
324 fayalite (<2.5 modal %) up to 3 mm in size, with thick alteration rims, complete the phase
325 assemblage. Glomeroporphyritic crystal clots are common (**figure 2e**). The fine-grained
326 (containing crystals up to 10 μm in size) groundmass is made up of a similar assemblage. The
327 rhyolite lava is dominantly aphyric, or crystal-poor porphyritic obsidian with <10 vol % crystals
328 held in a glassy groundmass (**figure 2f**). The phase assemblage is made up by euhedral
329 phenocrysts of sanidine (70 modal %), rounded quartz (15 modal %), and elongate or rounded
330 aegirine augite and aenigmatite (7 modal %), all up to 1 mm in size. Granophyric intergrowths of

quartz and alkali feldspar are common (**figure 2f**). At up to 2.5 mm in size, these intergrowths appear to nucleate around a grain showing dissolution textures, and can contain inclusions of aegirine-augite. They may represent growth during rapid undercooling of melt compositions that are under-saturated with respect to quartz (Gleeson et al., 2017; Lowenstern et al., 1997). The glass matrix of the rhyolites contains aligned microlites of alkali feldspar and aegirine augite. Post-caldera pumice deposits are similar in assemblage and petrographic texture to the post-caldera rhyolite lavas, though generally have lower phenocryst contents (closer to aphyric).

4.2 Whole-rock and glass compositions

4.2.1 Major elements

Whole-rock compositions for Kone and Fentale are presented in **table 1 and provided in supplementary 12 and supplementary 13**, glass compositions for Aluto, Kone and Fentale are presented in **table 2** and provided in **supplementary 14**. Whole-rock compositions for Aluto volcanic products are presented by Hutchison et al. (2016c) and are highlighted by fields marked out by dashed lines. Rocks were classified using the total alkalis-silica (TAS) diagram (**figure 3a**) after LeBas et al. (1986), and the FeO_t – Al_2O_3 diagram (**figure 3b**) after Macdonald (1974). There is a large range in silica content across the sample suite, although rocks of intermediate composition are absent, the data show a clear gap in compositions between ~50 to 60 wt% SiO_2, excepting rare examples of enclaves from Aluto (Hutchison et al., 2016c). All of the evolved samples are peralkaline, with most classified as pantellerites based on their high FeO concentrations (**figure 3b;** Macdonald, 1974). Some Aluto trachytic ignimbrites appear comenditic due to their raised Al_2O_3 contents. The mafic samples have a transitional composition and straddle the alkaline-subalkaline divide of Irvine and Baragar (1971) (**figure 3a**).

Both the glass and whole-rock data show that increasing SiO_2 content correlates with an increase in alkalis and a decrease in ferromagnesian, Ca and Ti oxides (**figure 4**). This trend is indicative of protracted fractional crystallisation controlled by removal of olivine, clinopyroxene, plagioclase, Fe-Ti oxide, quartz, alkali feldspar and aenigmatite (in approximate order of appearance). K_2O shows a smooth, largely linear increase (**figure 4g**). Al_2O_3 shows flat but scattered levels before a step-change at ~68 wt. % SiO_2, where it decreases to 7.5–12 wt. % in the pantellerite samples, reflecting the dominance of alkali feldspar fractionation (**figure 4a**). Na_2O shows an increasing trend with SiO_2 up to the trachytic compositions, then displays considerable variation (2.5–7 wt. %) within the pantellerites (**figure 4f**). The variation in Na_2O after ~70 wt.% SiO_2 reflects the dominance of alkali feldspar as the fractionating phase, though it should be noted that glass alteration and Na loss may also be important. By comparing the FK/A indicator of peralkalinity (mol (Fe+K)/Al) to that of the agpaitic index (A.I.- mol (Na+K)/Al), several Kone samples, namely the silicic glasses, are identified as likely to have undergone Na loss (see **supplementary 1**) (White et al., 2003). Hutchison et al. (2016c) examined Na loss at Aluto in samples collected from isolated pumice cones that would have been located at the edge of the lake during lacustrine high stands, leading them to suggest that post-emplacement alteration processes (e.g., leaching by surface water interaction) may be the causal factor. Na loss has also been identified in pumice from Rungwe, Tanzania, Fontijn et al. (2013) suggest that the combination of high vesicularity, increasing exposed surface area, and the climate contributes to the alteration.

Whilst the glass and whole-rock data are generally tightly coupled, the glass data shows slightly lower MgO and FeO, and higher TiO_2 and K_2O at the mafic end of the spectrum, and higher SiO_2 and Na_2O at the silicic end of the spectrum, particularly compared to whole-rock analyses of the crystal-rich ignimbrites. This likely reflects the presence of retained, large olivine phenocrysts in the basalts, and alkali feldspar phenocrysts in the pantellerites. Peralkaline melts become increasingly sodic as they evolve due to the 'orthoclase effect' (Bailey & Schairer, 1964). Gibson (1974) identified significant geochemical variation between Fentale pre- and post-caldera pantellerites, this study replicates that with post-caldera samples showing higher SiO_2 and lower TiO_2, FeO, MnO contents noted in both the whole-rock and glass data. No such pattern was observed for the Kone samples.

Best-fit RhyoliteMELTS models (Gualda et al., 2012) for Kone and Fentale were determined using least squares residual analysis (following the method of Gleeson et al., 2017), these are plotted as solid lines, along with the model for Aluto determined by Gleeson et al. (2017) (**figure 3 and 4**). The models provide a good first-order fit to the geochemical data, but deviation is observed for more evolved (pantelleritic) compositions. There is a departure of the model from FeO, CaO, Na_2O and P_2O_5 glass and whole-rock compositions (**figures 4c, 4e and 4h**) and consequently the model overestimates peralkalinity substantially for the rhyolites with SiO_2 > 70 wt%. Over-prediction of P_2O_5 and CaO is likely related to inaccuracies in the stabilisation of apatite and other mineral phases for which Rhyolite-MELTS is not calibrated (Rooney et al., 2012). Under-prediction of FeO content reflects the limited constraint on aenigmatite stability (Hutchison et al., 2018). Rooney et al (2012) highlight the lack of experimental constraints on the stability of F-bearing phases in thermodynamic models for peralkaline systems.

4.2.2 Trace Elements

The co-variation of selected trace elements with Zr, which is highly incompatible in peralkaline melts (**figure 5a**), is shown in **figure 5**. Compatible elements show a negative correlation with Zr (**figure 5b and 5c**); incompatible elements show a positive correlation. Incompatible-incompatible trace element diagrams (**figure 5d-g**) show linear positive trends that pass through the origin, and are consistent with the most evolved compositions at Aluto, Kone, and Fentale being derived from a mafic parent similar to those sampled. Incompatible element ratios such as Rb/Nb (**figure 5h**) do not show significant variability across the sample suite. Rb/Nb ratios are generally lower in the sample suite than that of the Precambrian crustal rocks (Peccerillo et al., 1998), which likely represent a component of the basement rocks.

Glass and whole-rock compositions are tightly coupled. Ba contents deviate from the other elements analysed, showing an increase in concentrations up to trachytic compositions, and then considerable variation (12–850 ppm) within the pantellerites (**figure 5c**), marking the appearance of alkali feldspar as a major fractionating phase. There is no clear relationship between the Ba concentrations observed in the whole-rock and in glass (**figure 5c**). Given the textural evidence of glomerocrystic clots of feldspar phenocrysts this may indicate accumulation of trace-element-enriched feldspar crystals (see section 5.3). Again, this study confirms the result of Gibson (1974), identifying differences between the trace element geochemistry of Fentale pre- and post-caldera pantellerites. Post-caldera samples have higher whole-rock and glass

concentrations of incompatible elements such as Y, Nb, La, and Rb, but lower concentrations of Ba. No such pattern was observed for the Kone samples.

4.3 Feldspar compositions

Plagioclase compositions in the Aluto samples include bytownite and labradorite (An_{55-81}; Ab_{42-18}; Or_{1-3}), whilst Kone samples are dominated by bytownite (An_{80-84}; Ab_{19-15}; $Or_{0-1.}$) (**figure 6**). Aluto trachytes contain feldspars that straddle the oligoclase/anorthoclase boundary (An_{5-42}; Ab_{77-56}; Or_{3-24}), with some rare andesine cores. Kone and Fentale samples contain minor amounts of these feldspars (An_{11-20}; Ab_{73-72}; Or_{8-18}). Alkali feldspars at Aluto are predominantly sanidine ($An_{0.1-0.4}$; Ab_{68-50}; Or_{32-65}), whilst at Kone and Fentale they straddle the anorthoclase/sanidine boundary ($An_{0.1-3}$; Ab_{76-54}; Or_{24-46}). Whilst some anorthoclases in both Kone and Aluto caldera-forming eruptive deposits display normal zoning, with more albitic cores (**figure 2b**), most show no apparent zoning (**figure 2c-f and 7a and 7b**); the range from core to rim is typically <3 mol% for Or and Ab. The feldspar analyses can be found in **table 3** and **supplementary 15 and supplementary 16.**

The predicted feldspar compositions from the best-fit RhyoliteMELTS models (Gleeson et al., 2017; Gualda et al., 2012) are shown plotted as solid lines on **figure 6**. They provide a good first-order fit to the geochemical data, following the smooth curve displayed by the observed plagioclase data closely. However, RhyoliteMELTS fails to accurately predict the composition of the alkali feldspars, over-predicting Or contents. The modelled fractionation of more potassic feldspars results in RhyoliteMELTS overestimating peralkalinity, as the influence of the orthoclase effect (Bailey & Schairer, 1964) is inflated.

Ba concentrations were used to assess trace element variation in the feldspars from the evolved rocks as Ba partitions strongly into the mineral phase and, unlike Sr, was observed above detection limits in most cases for the alkali feldspars. Data is presented in **table 3**. The oligoclase and anorthoclase plagioclase feldspars typically contain the highest Ba concentrations, reaching >4000 ppm Ba. Alkali feldspar Ba contents are highly variable at the individual sample scale for each of the volcanoes investigated, with an average standard deviation of 339 ppm for the Aluto samples, 266 ppm for the Kone samples, and 453 ppm for the Fentale samples. It should be noted that every sample also contained feldspars with Ba concentrations below the detection limits so the actual variation is larger. Individual samples contain feldspars with a standard deviation in Ba concentration of up to 853 ppm, with Ba concentrations varying between several hundred ppm and >4000 ppm. Variation in Ba concentrations tends to be greatest within the samples erupted during caldera-formation; and these samples also contain the most crystals with Ba concentrations above detection limits. Evidence for zoning was limited within the alkali feldspars (**figure 7a and b**). Where zoning in major elements exists there is no systematic change in Ba contents from core to rim (**figure 7a**). The limited amount of zoning observed may have been acquired from a range of processes (i.e., feldspar growth in a progressively evolving liquid, diffusive re-equilibration of crystals scavenged from a geochemically distinct region). Only the rims, and their relationship to their carrier liquids, are examined further in this study (note that in most cases the rims and cores are identical; **Figure 7**).

460

461 **5 Discussion**

462 5.1 Magma compositions are dominated by a fractional crystallisation signature

463 As has been proposed in previous studies (e.g. Giordano et al., 2014; Hutchison et al.,
464 2016c; Hutchison et al., 2018; Macdonald et al., 2011; Peccerillo et al., 2003), the whole-rock
465 and glass data are consistent with pantelleritic magmas being derived via extreme fractional
466 crystallisation of a basaltic parental melt. Following the method of Gleeson et al. (2017) for
467 Aluto (for full details see **supplementary 2 and 3**), least squares residual analysis was used to
468 find the best fit RhyoliteMELTS models (Gualda et al., 2012) for Kone and Fentale, using
469 basalts from these volcanoes as starting compositions (samples MER133A and F12). There are a
470 number of initial conditions which appear to provide a reasonably good match to the
471 compositional data, however results of the statistical analysis indicate that fractional
472 crystallisation at low pressure conditions (100 MPa), fO_2 at the QFM-QFM+1 buffer, and an
473 initial water content of ~1 wt% offer the best-fit RhyoliteMELTS models for Kone and Fentale
474 volcanoes. This is consistent with the best-fit model presented by Gleeson et al. (2017) for Aluto,
475 and with findings for other peralkaline centres along the MER and globally (e.g. Barberi et al.,
476 1975; Gasparon et al., 1993; Hutchison et al., 2018; Peccerillo et al., 2003; Neave et al., 2012;
477 Rooney et al., 2012).

478 Some authors have suggested that peralkaline magmas may be generated by melting of
479 pre-existing basaltic rocks (Beard & Lofgren, 1991; Garland et al., 1995; Hay & Wendlandt,
480 1995; Thy et al., 1990). However, trace element ratios are constant through the differentiation
481 suite and are also much lower than those of the local Precambrian crust (**figure 5h**). Peccerillo et
482 al. (2003) suggest that partial melting of crustal rocks would tend to increase melt large ion
483 lithophile and high field strength element ratios (LILE/HFSE, e.g., Rb/Nb) making it unlikely
484 that there has been significant contribution from crustal assimilation. Hutchison et al. (2018)
485 used Sr-Nd-O isotope systematics to rule out major crustal assimilation at both Kone and Aluto,
486 consistent with these findings.

487

488 5.2 Implications for our understanding of Daly Gap formation

489 There is a total absence of eruption deposits at Kone and Fentale with the intermediate
490 magma compositions which are predicted to form during protracted fractional crystallisation.
491 This compositional gap is often referred to as the 'Daly Gap' (Daly, 1925) and has also been
492 noted at Aluto (Gleeson et al., 2017; Hutchison et al., 2016c) where only rare enclaves, thought
493 to be the product of magma mixing (Hutchison et al., 2016c) have intermediate compositions.
494 The 'Daly Gap' has been observed at other sites along the MER (Peccerillo et al., 2003; Ronga et
495 al., 2009; Rooney et al., 2012), and at other peralkaline systems globally (Neave et al., 2012;
496 White et al., 2009). The 'Daly Gap' is often used to argue against derivation of peralkaline
497 liquids by protracted fractional crystallisation (e.g. Chayes, 1963; 1977). Despite this challenge,
498 the feldspar data collected for Aluto, Kone and Fentale preserve evidence for crystallisation of
499 magmas of intermediate composition somewhere in the storage system. The smooth change in
500 feldspar major element compositions observed in the samples analysed is further supported by
501 the RhyoliteMELTS simulations of fractional crystallisation, which closely replicate plagioclase
502 feldspar evolution (**figure 6**). The majority of the andesine and oligioclase analyses were taken

from resorbed feldspar cores, rimmed by more potassic compositions (**figure 2b and 2c**), providing geochemical evidence for crystallisation of intermediate magmas prior to melt evolution. White et al. (2009) described anorthoclase phenocrysts from trachytes erupted at Pantelleria with similar plagioclase composition cores, suggesting that they may have formed from benmoreitic magmas, trapped in lower, dense and viscous portions of the storage system by a trachytic 'trap' zone. The 'filtering' effects of density stratified peralkaline magma reservoirs have previously been cited as a mechanism for 'Daly Gap' formation at Aluto (Gleeson et al., 2017), as well as Gedemsa (Peccerillo et al., 2003) volcano in the MER. Careful examination of the Fentale welded tuff by Gibson (1974) has revealed that it was erupted from a compositionally- and therefore likely density-stratified storage region.

The best-fit RhyoliteMELTS models for Aluto (Gleeson et al., 2017), Kone, and Fentale suggest, in addition, that these compositions may be physically scarce, with fractionating magmas passing rapidly through the intermediate stages. The models show that SiO_2 does not vary linearly with temperature (**figure 8a**) or melt fraction (F) (**figure 8b**), which corresponds to the degree of crystallisation (1-F). Mushkin et al. (2002) presented an equation for estimating the rate of change of differentiation:

$$\frac{\partial SiO_2}{\partial t} \propto \frac{\partial SiO_2}{\partial H}(T_m - T_0)V^{\frac{2}{3}} \qquad \textbf{(1)}$$

, where $\frac{\partial SiO_2}{\partial t}$ is the rate of change of SiO_2, H is the released heat at each melt temperature (T_m) and V is the melt volume. The wall rock temperature (T_0) has been varied as it is not output from the RhyoliteMELTS models. The models predict that faster rates of differentiation occur between ~50 to ~65 wt% SiO_2 (**figure 8c**). This has been suggested as the result of separation of SiO_2-poor minerals over this narrow interval (Clague, 1978; Gleeson et al., 2017; Peccerillo et al., 2003). This rapid differentiation may aid preservation of the plagioclase feldspar cores observed at Aluto, Kone, and Fentale, with timescales too short for complete re-equilibration. The occurrence of the 'Daly Gap' is likely due to a combination of factors, including the predicted scarcity of intermediate compositions produced during fractionation, and the density stratification of zoned storage systems that may keep potentially crystal-rich zones of intermediate magmas locked away.

5.3 Heterogeneous crystal cargoes: evidence for entrainment of antecrysts

While the whole-rock and glass geochemistry displays clear trends related to fractional crystallisation, there is significant heterogeneity in the trace element composition of the feldspars (**figure 9**). The Ba concentrations in the rims of individual feldspars within a sample can vary greatly, reflected in the unsystematic divergence between whole-rock and glass measurements of feldspar compatible traces such as Ba (**figure 5c**). This suggests that a portion of the feldspars are antecrystic, particularly within the crystal-rich ignimbrite samples, where glomerocrystic clots of crystals, consistent with this interpretation, are prevalent. While phase equilibria will maintain alkali feldspar compositions at around Or 35±5% for evolved peralkaline melts (Bailey, 1974; Bailey et al., 1974; Bailey & Schairer, 1964; Carmichael & MacKenzie, 1963; Nicholls & Carmichael, 1969; Thompson & MacKenzie, 1990), the trace element contents of the feldspars

545 are expected to vary as crystallisation continues owing to the relatively large changes in trace
546 element concentrations in melts during crystallisation (and changing partitioning behaviour with
547 temperature and melt composition). Therefore, detailed trace element analysis is needed in order
548 to reveal the true complexity of feldspars in these systems.

549 Ba partitioning between feldspar and peralkaline silicate melt depends largely on
550 temperature and melt composition (in particular peralkalinity) (Henderson & Pierozynski, 2012).
551 It has been suggested that Ba feldspar-melt partition coefficients drop steeply with peralkalinity,
552 despite the accompanying modest increases in SiO_2 and drop in temperatures (Henderson &
553 Pierozynski, 2012; Mahood & Stimac, 1990). This is due to increasing melt SiO_2 content being
554 accompanied by a decline in network-forming Al and an increase in Fe content, leading to Ba
555 becoming very incompatible in feldspar crystals in highly evolved peralkaline melts. Here we
556 have predicted melt Ba contents from the observed feldspar rim trace element geochemistry. Ba
557 alkali feldspar-melt partition coefficients (D_{Ba}) are based on **equation 2** from the experimental
558 work of Henderson and Pierozynski (2012):

559

560 $$\ln(D_{Ba}) = 37.8 - 0.06NKA - 0.037T \quad \textbf{(2)}$$

561

562 , where NKA is the glass peralkalinity ($Na_2O + K_2O)/Al_2O_3$, mol%), temperature was set at 765
563 °C (Gleeson et al., 2017). **Figure 9** shows that in many cases the predicted melt Ba value is
564 much higher than that of the observed, indicating that the feldspars are not in equilibrium with
565 their carrier melt. As the partition coefficients calculated by this method are strongly dependent
566 on melt peralkalinity it should be again be noted that several Kone samples may have low NKA
567 due to Na loss (**supplementary 1;** White et al., 2003). Partition coefficients calculated for these
568 samples may therefore be much higher than the true values and will produce lower predicted
569 melt Ba concentrations. An adjusted value, based on the relationship between the FK/A and A.I.
570 indicators of peralkalinity (White et al., 2003) has also been used in these calculations, producing
571 more reasonable predicted melt Ba in these cases. Melt Ba contents based on the 'effective'
572 partition coefficients, observed in natural samples, of Mahood and Stimac (1990) are also
573 indicated by the thick solid lines. The lower D_{Ba} of 1.2 is largely consistent with the relationship
574 between the observed feldspar and melt Ba contents, however the higher D_{Ba} of 5.9 given by
575 Mahood and Stimac (1990) again predicts much higher melt Ba contents based on the feldspar
576 rims.

577 Ba partitioning behaviour between alkali feldspars and melt, as constrained by Henderson
578 and Pierozynski (2012), was also used to produce a simple fractional crystallisation model based
579 on RhyoliteMELTS simulations (Gualda et al., 2012) of the liquid line of descent (shown in
580 **figure 3 and 4**). Partition coefficients are calculated using **equation 2** for each major element
581 melt composition produced by RhyoliteMELTS, which are then converted to bulk partition
582 coefficients using the mineral assemblages output by RhyoliteMELTS, assuming negligible
583 intake of Ba by phases other than feldspar. This bulk partition coefficient is then input into a
584 fractional crystallisation equation:

585

586 $$\frac{C_i^l}{C_i^o} = (1 - X)^{D-1} \quad \textbf{(3)}$$

587

588 , where i is the element of interest, C^o is the original concentration in the parental liquid, taken
589 from the Ba contents of the starting basalts input into RhyoliteMELTS (17-01-05 for Aluto,
590 MER133A for Kone, F12 for Fentale), C^l is the concentration in the liquid, D is the solid-melt
591 partition coefficient, F is the melt fraction, and X is the fraction of material crystallised.

592 The results of the modelling are shown in **figure 10**, along with the observations from the
593 Aluto, Kone and Fentale samples, and the experimental glasses on which the Ba feldspar-melt
594 partitioning behaviour is based (Henderson & Pierozynski, 2012) as well as some natural Ba data
595 for pantellerite samples (Mahood & Stimac, 1990). The feldspar-melt partition coefficients for
596 Ba (D_{Ba}), predicted by RhyoliteMELTS combined with the empirical Ba partitioning behaviour
597 described by Henderson & Pierozynski (2012), extend only up to 0.5 for the evolved
598 compositions investigated, quickly dropping again as the SiO_2 content, and consequently the
599 peralkalinity, increases (**figure 10c and 10d**). These very low partition coefficients mean that the
600 model predicts the Ba content of the melt to rise rapidly (**figure 10b**) and feldspar Ba contents to
601 peak at only 1000 ppm (**figure 10a**). The Fentale model predicts much lower values for D_{Ba}, and
602 consequently the feldspars too. However, it is likely that these model partition coefficients are
603 too low, due to the overestimation of melt peralkalinity in RhyoliteMELTS. We believe that
604 observations of Ba partitioning in the experimental glasses of Henderson & Pierozynski (2012)
605 and the natural unzoned pantelleritic samples of Mahood and Stimac, (1990) produce more
606 realistic estimates of partition coefficients (**figure 10**).

607 The natural data from the MER volcanoes show high and variable feldspar rim Ba
608 concentrations (**figure 10a**), and melt Ba concentrations of 60 to 850 ppm (**figure 10b**), thereby
609 yielding higher and more variable 'apparent' feldspar-melt partition coefficients, calculated
610 using feldspar rim values and average melt compositions, than predicted. This is particularly
611 notable in samples from eruptions associated with caldera-forming events (**figure 10c and 10d**).
612 Mahood and Stimac (1990) produced *observed* partition coefficients for five pantellerites and
613 trachytes from Pantelleria by averaging data from unzoned phenocrysts, the upper and lower
614 values of the range they calculated are shown on **figure 10c and 10d**. The majority of 'apparent'
615 partition coefficients calculated for the MER volcanic samples fall within this range, and
616 therefore so do the averaged observed partition coefficient for each sample. However, the spread
617 of 'apparent' coefficients is large, producing large standard deviations, particularly for the
618 caldera-forming samples which show can show a σ of up to 5.5 (**table 3**). Mahood and Stimac
619 (1990) cite zoning as the likely cause of variability in literature values for feldspar-melt Ba
620 partition coefficients, however this has been ruled out in this study by only using rims of crystals
621 that appear themselves to be unzoned (**figure 7a and b**). It should also be noted that the data do
622 not show a fall in the partition coefficients, predicted for increasingly evolved (**figure 10c**),
623 increasingly peralkaline melts (**figure 10d**) (Henderson & Pierozynski, 2012; Mahood & Stimac,
624 1990). However these studies were limited to rhyolites with <70 wt% SiO_2, and may not be
625 representative of the high silica rhyolites we present.

626 We interpret these data (shown in **figures 9 and 10**) to show that a portion of the Ba-rich
627 feldspars, particularly within the caldera-forming ignimbrite deposits, are antecrysts, crystallised
628 from a Ba-rich (more primitive) melt, before being entrained into a Ba-depleted (more evolved)
629 melt. One interpretation of this observation is that these antecrysts, during the process of
630 fractional crystallisation, were segregated from the melt and stored in a distinct region of the
631 magma reservoir. This crystallisation and segregation of alkali feldspars would continually strip

the melt of compatible elements, such as Ba, sequestering them in the crystals. At some point before or during eruption, the melt entrained these crystals, which may have been disaggregated from a crystal-rich region of the reservoir. Textural evidence of mush disaggregation can be observed in the prevalence of glomerocrystic clots of feldspars in the crystal-rich ignimbrites. We propose a conceptual structure for the peralkaline magma reservoirs beneath Aluto and Kone that is consistent with the evidence we present here (**figure 11)**. The reservoir may contain feldspar-rich 'mush' regions, with segregated residual liquids in the upper portions. This structure is consistent with the hypothesis that the 'Daly Gap' may be caused by density filtering, with less evolved magmas locked away in crystal-rich mushes (see section 5.2). Post-caldera eruptions primarily tap the residual liquids, with relatively low fractions of antecrysts, whilst more explosive, larger volume eruptions, associated with caldera-forming events, may excavate a mush pile, erupting a cargo of more Ba-enriched crystals out of equilibrium with the carrier liquid (**figure 9 and 10a)**. The absence of notable trace element zoning in the antecrysts (**figure 7a and 7b**) suggests that conditions are not suitable for rim growth and/or the timescale between crystal accumulation and eruption is short. Ba is a slow diffusing element (Cherniak, 2002) which would require the timescales for equilibration to be long: equilibration of 100 micron thick rims at 700 °C would require timescales of Ma (Cherniak, 2002). It may be that long-term storage in a 'mush region' has resulted in the diffusive homogenisation of the crystals, removing any zoning developed during growth in a continually evolving liquid, prior to incorporation into their final carrier liquid. We speculate that this crystal scavenging may have taken place during eruption, although the timing of it remains unconstrained.

High crystallinity 'mush' bodies have been inferred to exist in the crust beneath other volcanoes in the EAR. Rooney et al. (2012) invoked a crystal-mush model to explain the chemical heterogeneity of the crystal cargo at Chefe Donsa. Macdonald et al (2008) observed cumulate feldspar-rich xenoliths enriched in Ba, Sr and Eu at peralkaline centres in the Kenyan Rift, whilst the elevated Ba contents of some melts from the Olkaria Volcanic Complex, Kenyan Rift, have been linked to resorption of remobilised alkali feldspars (Macdonald et al., 2012). Marshall et al (2009) also observed disequilibrium features in phenocrysts that were tentatively linked to crystal scavenging at Olkaria. At Menengai volcano, there is isotopic consistency between phenocrysts that are out of equilibrium with their carrier melts in terms of trace elements, indicating a common genetic source for the antecrysts (Macdonald et al., 1994). Gibson (1974) also suggested that the differing geochemistry of pre- and post-caldera deposits at Fentale volcano may even relate to the loss of 'fugitive material' during large caldera eruptions. The data from this study supports this link, with lower Ba concentrations observed in the Fentale post-caldera whole-rock, glass and feldspar analyses. The absence of this pattern at Kone may be related to the volcanoes history of multiple caldera eruptions, where pre-Kone caldera samples may also be viewed as post-Birenti caldera samples. The only non-caldera sample to contain feldspars with significant Ba concentrations was the singular pre-Birenti obsidian investigated.

5.4 Timescales of crystal settling and compaction in a peralkaline magma reservoir

Segregation of liquids and crystals during protracted fractional crystallisation is an important process in the evolution of Aluto, Kone, and Fentale peralkaline magmas. Our data suggest that residual melts are stripped of compatible trace elements, such as Ba, which are sequestered in feldspars in crystal mush piles (**figure 11**). Observations of crystal-poor peralkaline rhyolites erupted between caldera-forming events requires the segregation of liquids

677 from crystals on timescales at least reflecting the inter-eruption periods. The efficiency of
678 settling and compaction may be aided by the relatively low viscosity of peralkaline melts: at 800
679 °C the Cuddia di Mida pantellerite viscosity lies between 5×10^3 and 5×10^4 Pa s for H_2O
680 concentrations of 2.5-4.9 wt% (Neave et al., 2012). This low melt viscosity promotes magma
681 differentiation and stratification through crystal settling; Stokes settling velocities of 10, 190 and
682 230 Ma^{-1} were reported for 1 mm grains of plagioclase, augite and olivine (Neave et al., 2012).

683 Here we calculate the timescales necessary for melt segregation in a peralkaline system
684 similar to Aluto following the method of Bachmann and Bergantz (2004) (for details of the
685 modelling see **supplementary 4-6;** Barnea & Mizrahi, 1973; Davis and Scrivos, 1985;
686 Jackson et al., 2003; McKenzie, 1984; Rabinowicz et al., 2001; Shirley, 1986). A melt viscosity
687 of 10^2 Pa s was used for the peralkaline melt, based on the model of di Genova et al. (2013) for a
688 melt with 5 wt. % H_2O and a temperature of 765°C, values which are considered representative
689 for MER volcanics (Gleeson et al., 2017; Webster et al., 1993). We assume a density contrast
690 between melt and crystals of 170 kg/m^3, based on the dominance of alkali feldspar (2550-2630
691 kg/m^3) and quartz (2650 kg/m^3), and a melt density of 2390 kg/m^3 (following Bottinga & Weill,
692 1970). All particles are assumed to be spherical and therefore these timescales are minima owing
693 to the decrease in settling velocity within a fluid with departure of a grain from a spherical shape
694 (Komar & Reimers, 1978). Porosity was set at 50% for compaction calculations based on
695 estimates of when a rigid crystal framework is formed for spherical particles (Vigneresse et al.,
696 1996); crystal fraction was set at 10% for hindered settling calculations based on the upper end
697 of phenocryst contents in post-caldera eruption deposits; see **supplementary 7 and 8** for the
698 effect of varying these parameters. Magma reservoir geometries were calculated assuming an
699 elliptical cylinder. The elliptical cross section had a long axis of 8 km and short axis of 5 km, in
700 line with the estimate of caldera size by Hutchison et al. (2015). There is considerable
701 uncertainty on the estimate of reservoir size. If the elliptical cross section used has 50% less area
702 then all estimates of compaction timescales will be an order of magnitude faster, whilst all
703 estimates of hindered settling will be two times slower (see **supplementary 9**). The model set-up
704 is shown in **supplementary 5**. Timescales of melt segregation for a metaluminous rhyolite melt
705 were modelled for comparison. Melt viscosity in this case was assumed to be 10^5 Pa s, assuming
706 a similar melt temperature and water content (Scaillet et al, 1998).

707 Mean eruption intervals at Aluto have been estimated at 300-400 years for post-caldera
708 pantellerites (**figure 12**; Fontijn et al., 2018). We calculated the timescales required to segregate
709 0.01 km^3 and 1 km^3 of melt, consistent with the range in eruptive volumes of crystal-poor post-
710 caldera eruptions at Aluto. For a mean grain size of 0.2 mm, it would take on the order of months
711 to tens of years to segregate 0.01 km^3 melt (**figure 12**), and tens of years to 10,000s of years to
712 segregate 1 km^3 melt from a crystalline mush, if we treat the magma reservoir as one coherent
713 body. The eruption intervals are typically greater than the upper limits required for melt
714 segregation suggested by the calculations, implying that there is sufficient time between
715 eruptions to extract enough melt for a post-caldera eruption of crystal-poor magma. It must be
716 stressed that this is a simple model, it may be that there are multiple regions of melt
717 accumulation in the reservoir, which would then decouple the eruption frequency from the time
718 scale needed to accumulate a particular volume of melt. Our results do highlight however, that
719 crystal-melt segregation is faster for peralkaline systems, with more than an order of magnitude
720 difference between the timescales versus a metaluminous system (**figure 12**).

721

5.5 Pre-eruptive Magma Storage Conditions

The pre-eruptive melt temperature of the Kone basaltic scoria was estimated using the clinopyroxene-liquid thermobarometer of Neave and Putirka (2017) (see **supplementary 10 and 11** for further details). Clinopyroxene-melt equilibrium was last achieved at a temperature of 1150-1170 ± 60 °C and pressures of 420-575 ± 140 MPa, equivalent to a depth of 15-21 ± 5 km assuming an average crustal density of 2800 gm^{-3} (Wilks et al., 2017). The Fe-Mg partitioning relationship between clinopyroxene and melt was used to select appropriate crystal rims for analysis. Observed partition coefficients (D_{Fe-Mg}) between the pyroxenes melt all lay within error of the 0.27 equilibrium value (Putirka, 2008).

The pre-eruptive temperature of the pantellerites at Aluto was estimated by Gleeson et al. (2017) at 718-765±23°C using an alkali feldspar thermometer (Purtika, 2008) and assuming an equilibration pressure of 150 MPa based on estimates using RhyoliteMELTS models (Gualda et al., 2012). These pressures convert to depths of 5.4 ± 1 km assuming an average crustal density of 2800 gm^{-3} (Wilks et al., 2017). Experimental studies have shown that the phase assemblage of alkali feldspar, clinopyroxene, aenigmatite, and ilmenite is stable at 1.0-1.5 kbar at near H_2O-saturated conditions and temperatures of 680-725 °C (di Carlo et al., 2010), largely consistent with the Aluto observations. Further North, in the Afar region, Field et al (2012) analysed melt inclusions from the peralkaline Dabbahu volcano, finding volatile saturation pressures in the range of 43-207 MPa, also consistent with shallow magma storage, at ~1-5 km depth in the crust.

However it should be noted, concerning temperature estimates, that we have highlighted complex crystal cargoes in pantellerite samples at Aluto, containing numerous alkali feldspars that are likely to be out of equilibrium with their host melts. These can often be difficult to identify based on petrographic observations and major-element analysis alone. If temperatures are higher than estimated by Gleeson et al. (2017), calculated feldspar-melt Ba partition coefficients will be lower, and thus predicted melt Ba based on feldspar rim compositions will be higher. If lower than estimated, partition coefficients will be higher and predicted melt Ba contents lower.

6 Implications of our study for geophysical imaging of peralkaline magma reservoirs

Whilst whole-rock and glass compositions of erupted products from Aluto, Kone, and Fentale reflect prolonged fractional crystallisation (**figures 3-5**), trace element heterogeneity in the crystal cargoes (**figure 9 and 10a**) is indicative of more complex processing including mixing and crystal scavenging, perhaps from a mush-dominated magma storage system. In support of a mush-dominated system, low-viscosity peralkaline liquids allow for efficient crystal-melt segregation, (**figure 12**) building mush piles where intermediate composition melts are locked away, and compatible elements, such as Ba, are sequestered. We suggest that crystal-rich ignimbrites, associated with caldera-forming events, may be able to scavenge Ba-enriched antecrysts from this region (**figure 11**). Post-caldera eruptions primarily tap residual melt, segregated in small melt lenses in the upper portions of the reservoir, with a much lower fraction of scavenged antecrysts.

Magnetotelluric surveys, used for inferring the Earth's subsurface electrical conductivity, have been conducted at several sites along the EARS (Desissa et al., 2013; Hübert et al., 2018; Johnson et al., 2015; Samrock et al., 2015 Whaler & Hautot, 2006). Resistivity is sensitive to

765 fluid content, allowing the method to identify the presence of partial melt beneath volcanoes
766 (Desissa et al., 2013; Johnson et al., 2015). However, the electrical conductivity of magmatic
767 reservoirs is dependent on the state of the magma itself, in terms of melt volatile abundance,
768 temperature, composition, and crystal content (Gaillard & Iacono Marziano, 2005). The
769 electrical conductivity of silicate liquids varies within a range of 10^{-2}-10^{1} ohm m^{-1} (Gaillard,
770 2004; Tyburczy & Waff, 1985; Waff & Weill, 1975), whilst the conductivity of crystals can be
771 in the range of 10^{-10}-10^{-3} ohm m^{-1} (Huebner & Dillenburg, 1995), making them insulators. A
772 highly crystalline mush, with a low melt fraction, may appear as a resistive structure (Hübert et
773 al., 2018). Indeed, despite the petrological estimates for shallow magma storage at Aluto
774 (Gleeson et al., 2017), as described above, magnetotelluric methods have not identified an area
775 of increased electrical conductivity in the crust (Hübert et al., 2018; Samrock et al., 2015) that
776 might indicate the presence of partial melt (e.g., Pous et al., 1999; Hoffman-Rothe et al., 2011;
777 Schilling & Partzsch, 2001). At shallow depths a conductive clay cap to the hydrothermal system
778 is proposed, whilst at greater depths the crust appears increasingly resistive (Hübert et al., 2018;
779 Samrock et al., 2015).

780 Small lenses of residual melt in the upper part of the system, which we hypothesise feed
781 the crystal-poor post-caldera eruptions, accumulate over short timescales (10^{-1}-10^{1} years). Small-
782 volume liquid lenses may be difficult to capture and resolve using conductivity surveys due to
783 the inherently low spatial resolution of the technique. The ephemeral nature of these liquid lenses
784 poses new challenges when imaging and monitoring peralkaline magmatic-volcanic systems,
785 with a need to better understand the limits of detection and the time-dependent evolution of
786 magmatic storage regions. The presence of a conductive anomaly at Boset-Bericha volcano
787 (Whaler & Hautot, 2006), for example, may reflect the time-sensitive capture of short-lived melt-
788 lens, although it could also indicate the presence of a longer-lived more melt-rich, interconnected
789 system. The scenarios at both Aluto and Boset-Bericha are in stark contrast to electrical
790 resistivity surveys carried out further North in the Afar region. Here large regions of low
791 resistivity have been imaged reaching down to 35 km depth, interpreted as long-lived reservoirs
792 containing ~13% melt fraction and extending down into the mantle (Desissa et al., 2013).

793 Other geophysical data from Aluto are consistent with a magma reservoir system
794 extending to depths of 9 km and deeper. A local network of 12 seismometers was deployed at
795 Aluto between 2012 and 2014, detecting more than 2000 earthquakes in a 24-month period
796 (Wilks et al., 2017). A shallow zone (at 0-2 km) of high seismicity and high b-values (a
797 parameter describing the relative abundance of large to small magnitude events) likely
798 corresponds to the active hydrothermal system, while deeper events (2-9 km) reflect high strain
799 rates where magmatic fluids cause elastic deformation (Wilks et al., 2017). At depths greater
800 than 9 km the crust appears largely aseismic, interpreted as an area of underlying ductile
801 magmatic mush (Wilks et al., 2017). These interpretations are largely consistent with those
802 arising from InSAR observations of deformation at Aluto. A period of inflation in 2008 is best
803 explained by a deformation source at ~5.1 ± 0.5 km depth, thought to reflect fluid injection into
804 the roof zone of a magma storage region (Hutchison et al., 2016a). A subsequent period of long-
805 term subsidence was interpreted as magmatic degassing and depressurisation of the hydrothermal
806 system (Hutchison et al., 2016a). Mahatsente et al. (1999) additionally located a positive gravity
807 anomaly within the shallow crust beneath Aluto during a regional survey. This could be
808 consistent with the presence of crystalline magmatic intrusions, and may provide evidence for
809 density filtering of intermediate magmas forming a 'Daly Gap' at Aluto (see section 5.2). Mattia

et al. (2007) suggested that trapped high-density intermediate magmas at Pantelleria may contribute to the positive gravity anomalies observed there.

InSAR observations of the Afar region have also been used to suggest shallow magmatic storage beneath volcanoes such as Dabbahu (Field et al., 2012; Grandin et al., 2010; Wright et al., 2006). Here a broad area of uplift, ~20 km in diameter, was shown to be consistent with a modelled scenario of stacked sills at 1-6 km depth. Seismic data obtained during the same period of unrest indicated similar depths of storage (Ayele et al., 2007; Ebinger et al., 2008; Field et al., 2012). Whilst silicic centres in the Afar region, such as Dabbahu, may appear similar to those of the MER in terms of peralkaline compositions and shallow storage, contrasting crustal electrical resistivity again highlights key differences. In this more mature Afar rift, large volumes of partial melt are stored throughout the crust (Desissa et al., 2013), magma flux to the surface appears to be greater (Hutchison et al., 2018) and eruptions are more frequent. At least five eruptions have occurred in Afar during the period of modern remote sensing (e.g., Allard et al., 1979; Ayele et al., 2007; Ayele et al., 2009; Ferguson et al., 2010; Grandin et al., 2009; Wright et al., 2006; Yirgu et al., 2006) whereas none have occurred in the MER. Silicic magmatic plumbing in the Afar region is also clearly linked to the rifting cycle. For example, Wright et al. (2006) showed that much of the melt supplied to a major dyking episode in 2005 was sourced from shallow chambers beneath the Dabbahu and Gabho volcanoes. In Afar magma storage reservoirs appear to be more connected and, potentially, laterally extensive (Biggs et al., 2016; Ebmeier et al., 2018; Xu et al., 2017) compared to the MER, where we hypothesise small portions of melt stored in poorly connected, ephemeral lenses.

7 Conclusions

While whole-rock and glass compositions are modelled effectively by fractional crystallisation, this simple model cannot explain the trace element (Ba) heterogeneity observed in the crystal cargoes from eruptive products at Aluto, Kone, and Fentale volcanoes. Many of the feldspars, particularly in samples from caldera-forming eruptions, are antecrysts, crystallised from a Ba-enriched (more primitive) melt, before being segregated during the process of fractional crystallization, and later entrained in Ba-depleted (more evolved) residual liquids. We propose that these antecrysts are sourced from a crystal-rich region of the magma reservoir (perhaps a 'mush') that is excavated during the largest eruptions, creating crystal-rich trachytes and rhyolites typical of caldera-forming eruptions.

The low-viscosity nature of peralkaline rhyolitic liquids causes crystal-melt segregation to occur on faster timescales than for metaluminous rhyolites (which are more viscous). Separated crystals sequester compatible elements such as Ba, whilst residual melts continue to evolve, likely going on to feed post-caldera eruptions. The timescales necessary for the segregation of enough residual, eruptible melt to feed a crystal-poor post-caldera eruption (0.01-1 km^3) are short (10^1-10^4 years). These isolated melt lenses may be small and ephemeral, perhaps making them difficult resolve using geophysical techniques (seismic tomography, electrical conductivity). The interpretation that peralkaline systems may spend portions of their life cycle dominated by crystalline mushes helps reconcile contrasting geophysical data for Aluto.

Our study highlights the absence of experimental data for Ba partitioning behavior in silica-rich peralkaline melts; and the deficiencies in the RhyoliteMELTS model at reproducing peralkalinity for the rhyolitic end of the magma series. This causes partitioning models, which depend on peralkalinity, to consistently underestimate feldspar-melt partition coefficients for Ba

and feldspar Ba contents. A previous study suggested that Ba feldspar-melt partition coefficients drop steeply with peralkalinity despite accompanying modest increases in SiO_2 and drop in temperatures (Mahood & Stimac, 1990); however, this study, and the experimental data of Henderson and Pierozynski (2012), was limited to rhyolites with <70 wt% SiO_2. Petrological experiments on more evolved peralkaline magmas are needed to improve our understanding of Ba partitioning in peralkaline rhyolitic magmas.

Acknowledgments

We acknowledge the expertise and assistance provided by colleagues from Addis Ababa University and the kind permission of national and regional authorities during fieldwork and sample collection. We thank John White and Tyrone Rooney and two anonymous reviewers for their helpful reviews and encouragement. Data from this study can be found in the supplementary files. This project is funded by the Natural Environment Research Council grant NE/L013932/1 (RiftVolc).

References

Abebe, B., Acocella, V., Korme, T. & Ayalew, D. (2007). Quaternary Faulting and Volcanism in the Main Ethiopian Rift. *Journal of African Earth Sciences 48*, 115–124.

Acocella, V., Korme, T., Salvini, F. & Funiciello, R. (2002). Elliptic calderas in the Ethiopian Rift: control of pre-existing structures. *Journal of Volcanology and Geothermal Research 119*, 189–203.

Agostini, A., Bonini, M., Corti, G., Sani, F. & Mazzarini, F. (2011). Fault Architecture in the Main Ethiopian Rift and Comparison With Experimental Models: Implications for Rift Evolution and Nubia–Somalia Kinematics. *Earth and Planetary Science Letters 301*(3), 479–492.

Ayele, A., Jacques, E., Kassim, M., Kidane, T., Omar, A., Tait, S., Nercessian, A., et al (2007). The volcano-seismic crisis in Afar, Ethiopia starting September 2005. *Earth and Planetary Science Letters 255* (1-2), 177–187.

Ayele, A., Keir, D., Ebinger, C., Wright, T.J., Stuart, G.W., Buck, W.R., Jacques, E., et al. (2009). September 2005 mega-dike emplacement in the Manda-Harraro nascent oceanic rift (Afar depression). *Geophysical Research Letters 36*(20).

Bachmann, O. & Bergantz, G. (2004). On the Origin of Crystal poor Rhyolites: Extracted from Batholithic Crystal Mushes. *Journal of Petrology 45*(8), 1565–1582.

Bachmann, O. & Bergantz, G. (2008). The Magma Reservoirs That Feed Supereruptions. *Elements 4*(1), 17–21.

Bachmann, O., Dungan, M. & Lipman, P. (2002). The Fish Canyon Magma Body, San Juan Volcanic Field, Colorado: Rejuvenation and Eruption of an Upper-Crustal Batholith. *Journal of Petrology 43*(8), 1469–1503.

Bailey, D. (1974). Experimental Petrology Relating to Oversaturated Peralkaline Volcanics: A Review. *Bulliten of Volcanology 38*, 635–652.

Bailey, D., Cooper, J. & Knight, J. (1974). Anhydrous Melting and Crystallisation of Peralkaline Obsidians. *Bulliten of Volcanology 38*, 653–665.

Bailey, D. & Schairer, J. (1964). Feldspar-Liquid Equilibria In Peralkaline Liquids - The Orthoclase Effect. *American Journal of Science 262*, 1198–1206.

Barberi, F., Ferrara, G., Santacroce, R., Treuil, M. & Varet, J. (1975). A Transitional Basalt-Pantellerite Sequence of Fractional Crystallisation, the Boina Centre (Afar Rift, Ethiopia). *Journal of Petrology 16*(1), 22–56.

Barberi, F., Santacroce, R. & Varet, J. (1974). Silicic Peralkaline Volcanic Rocks of the Afar Depression (Ethiopia). *Bulliten of Volcanology 38*(2), 755–790.

Barclay, J., Carroll, M. R., Houghton, B. F., & Wilson, C. J. N. (1996). Pre-Eruptive Volatile Content and Degassing History of an Evolving Peralkaline Volcano. *Journal of Volcanology and Geothermal* Research 74, 75–87.

Barnea, E. & Mizrahi, J. (1973). A Generalized Approach to the Fluid Dynamics of Particulate Systems. Part I. General Correlation for Fluidization and Sedimentation in Solid Multiparticulate Systems. *Chemical Engineering Journal 5*, 171–189.

Beard, J. & Lofgren, G. (1991) Dehydration Melting and Water-Saturated Melting of Basaltic and Andesitic Greenstones and Amphibolites at 1, 3, and 6.9 Kb. *Journal of Petrology 32*(2), 365–401.

Biggs, J., Keir, D. & Lewi, E. (2011). Pulses of Deformation Reveal Frequently Recurring Shallow Magmatic Activity beneath the Main Ethiopian Rift. Geochemistry, Geophysics, Geosystems *12*(9), 1–11.

Biggs, J., Robertson, E. & Cashman, K. (2016). The lateral extent of volcanic interactions during unrest and eruption. *Nature Geoscience 9*, 308–311.

Bilham, R., Bendick, R., Larson, K., Mohr, P., Braun, J., Tesfaye, S. & Asfaw, L. (1999). Secular and tidal strain across the main Ethiopian rift. *Geophysical Research Letters 26*(18), 2789–2792.

Blake, S. & Ivey, G. (1986). Magma-Mixing and the Dynamics of Withdrawal from Stratified Reservoirs. *Journal of Volcanology and Geothermal Research 27*(1-2), 153–178.

Boccaletti, M., Getaneh, A., Mazzuoli, R., Tortorici, L. & Trua, T. (1995). Chemical Variations in a Bimodal Magma System: The Plio-Quaternary Volcanism in the Dera Nazret Area (Main Ethiopian Rift, Ethiopia). *Africa Geoscience Review 2*(1), 37–60.

Bonini, M., Corti, G., Innocenti, F., Manettie, P., Mazzarini, F., Abebe, T. & Pecskay, Z. (2005). Evolution of the Main Ethiopian Rift in the Frame of Afar and Kenya Rifts Propagation. *Tectonics 24*, 1–21.

Bottinga, Y. & Weill, D. (1970). Densities of Liquid Silicate Systems Calculated from Partial Molar Volumes of Oxide Components. *American Journal of Science 269*, 169–182.

Carmichael, I. & MacKenzie, W. (1963). Feldspar-Liquid Equilibria in Pantellerites: An Experimental Study. *American Journal of Science 261*, 382–396.

Cashman, K.V. & Giordano, G. (2014). Calderas and magma reservoirs. *Journal of Volcanology and Geothermal Research 288*, 28–45.

Cashman, K.V. & Sparks, R.S.J. (2013). How volcanoes work: A 25 year perspective. *Geological Society of America Bulletin 125*(5-6), 664–690.

933 Cashman, K., Sparks, R., & Blundy, J. (2017). Vertically Extensive and Unstable Magmatic
934 Systems: A Unified View of Igneous Processes. *Science 355*(6331), eaag3055.

935 Chayes, F. (1963). Relative abundance of intermediate members of the oceanic basalt-trachyte
936 association. *Journal of Geophysical Research 68*(5), 1519–1534.

937 Chayes, F. (1977). The oceanic basalt-trachyte relation in general and in the Canary Islands.
938 *American Mineralogist 62*, 666–671.

939 Cherniak, D. J. (2002). Ba diffusion in feldspar. *Geochim Cosmochim Acta 66*(9), 1641–1650

940 Chu, R., Helmberger, D., Sun, D., Jackson, J. & Zhu, L. (2010). Mushy Magma beneath
941 Yellowstone. *Geophysical Research Letters 37*, 1–5.

942 Clague, D. (1987). Hawaiian xenolith populations, magma supply rates, and development of
943 magma chambers. *Bulletin of Volcanology 49*(4), 577–587.

944 Cole, J. (1969). Gariboldi Volcanic Complex, Ethiopia. *Bulliten of Volcanology 33*, 566–578.

945 Cooper, K. & Kent, A. (2014). Rapid Remobilization of Magmatic Crystals Kept in Cold
946 Storage. *Nature 506*(7489), 480–483.

947 Corti, G. (2008). Control of rift obliquity on the evolution and segmentation of the main
948 Ethiopian rift. *Nature Letters 1*, 258–262.

949 Corti, G. (2009). Continental Rift Evolution: From Rift Initiation to Incipient Break-up in the
950 Main Ethiopian Rift, East Africa. *Earth Science Reviews 96*, 1–53.

951 Davis, R. & Scrivos, A. (1985). Sedimentation of Noncolloidal Particles at Low Reynolds
952 Numbers. *Annual Reviews in Fluid Mechanics 17*(1), 91–118.

953 de Silva, S., Salas. G. & Schubring, S. (2008). Triggering Explosive Eruptions—The Case for
954 Silicic Magma Recharge at Huaynaputina, Southern Peru. *Geology 36*(5), 387–390.

955 Desissa, M., Johnson, N. E., Whaler, K. A., Hautot, S., Fisseha, S. & Dawes, G. J. K. (2013). A
956 mantle magma reservoir beneath an incipient mid-ocean ridge in Afar, Ethiopia. *Nature*
957 *geoscience*, *6*(10), 861.

958 di Carlo, I., Rotolo, S., Scaillet, B., Buccheri, V. & Pichavant, M. (2010). Phase Equilibrium
959 Constraints on Pre-Eruptive Conditions of Recent Felsic Explosive Volcanism at Pantelleria
960 Island, Italy. *Journal of Petrology 51*(11), 2245–2276.

961 di Genova, D., Romano, C., Hess, K., Vona, A., Poe, B., Giordano, D., Dingwell, D., et al.
962 (2013). The Rheology of Peralkaline Rhyolites from Pantelleria Island. *Journal of Volcanology*
963 *and Geothermal Research 249*, 201–216.

964 Ebinger, C. J. (2005). Continental Break-Up: The East African Perspective. *Astronomy &*
965 *Geophysics 46*(2), 2–16.

966 Ebinger, C., Keir, D., Ayele, A., Calais, E., Wright, T.J., Belachew, M., Hammond, J.O., et al.
967 (2008). Capturing magma intrusion and faulting processes during continental rupture: seismicity
968 of the Dabbahu (Afar) rift. *Geophysical Journal International 174,* 1138-1152.

969 Ebmeier, S.K., Andrews, B.J., Araya, M.C., Arnold, D.W.D., Biggs, J., Cooper, C., Cottrell, E.,
970 et al. (2018). Synthesis of global satellite observations of magmatic and volcanic deformation:

971 implications for volcano monitoring & the lateral extent of magmatic domains. *Journal of*
972 *Applied Volcanology 7*(1), 2.

973 Ferguson, D.J., Barnie, T.D., Pyle, D.M., Oppenheimer, C., Yirgu, G., Lewi, E., Kidane, T.,
974 Carn, S. & Hamling, I. (2010). Recent rift-related volcanism in Afar, Ethiopia. *Earth and*
975 *Planetary Science Letters 292* (3), 409–418.

976 Field, L., Blundy, J., Brooker, R.A., Wright, T.J. & Yirgu, G. (2012). Magma storage conditions
977 beneath Dabbahu Volcano (Ethiopia) constrained by petrology, seismicity and satellite geodesy.
978 *Bulletin of Volcanology 74*(5), 981–1004.

979 Fontijn, K., Elburg, M. A., Nikogosian, I. K., van Bergen, M. J., & Ernst, G. G. (2013).
980 Petrology and geochemistry of Late Holocene felsic magmas from Rungwe volcano (Tanzania),
981 with implications for trachytic Rungwe Pumice eruption dynamics. *Lithos*, *177*, 34-53.

982 Fontijn, K., McNamara, K., Tadesse, A.Z., Pyle, D.M., Dessalegn, F., Hutchison, W., Mather,
983 T.A, et al. (2018). Contrasting styles of post-caldera volcanism along the Main Ethiopian Rift:
984 Implications for contemporary volcanic hazards. *Journal of Volcanology and Geothermal*
985 *Research* 356, 90-113.

986 Furman, T. (2006). Geochemistry of East African Rift basalts: An overview. *Journal of African*
987 *Earth Sciences 48*, 147–160.

988 Gaillard, F. (2004). Laboratory Measurements of Electrical Conductivity of Hydrous and Dry
989 Silicic Melts under Pressure. *Earth and Planetary Science Letters 218*(1-2), 215–228.

990 Gaillard, F. & Iacono Marziano, G. (2005). Electrical Conductivity of Magma in the Course of
991 Crystallisation Controlled by Their Residual Liquid Composition. *Journal of Geophysical*
992 *Research: Solid Earth 110*(B6), 1–12.

993 Garland, F., Hawkesworth, C. & Mantovani, M. (1995). Description and Petrogenesis of the
994 Paranà Rhyolites. *Journal of Petrology 36*(5), 1193–1227.

995 Gasparon, M., Innocenti, F., Manettie, P., Peccerillo, A. & Tsegaye, A. (1993). Genesis of the
996 Pliocene to Recent Bimodal Mafic-Felsic Volcanism in the Debre Zeyt Area, Central Ethiopia:
997 Volcanological and Geochemical Constraints. *Journal of African Earth Sciences 17*(2), 145–165.

998 Gibson, I.L.(1967). Preliminary Account of the Volcanic Geology of Fantale, Shoa. *Bulletin of*
999 *the Geophysical Observatory 10*, 59–67.

1000 Gibson, I. (1969). The Structure and Volcanic Geology of and Axial Portion of the Main
1001 Ethiopian Rift. *Tectonophysics 8*, 561–565.

1002 Gibson, I. (1970). A Pantelleritic Welded Ash-Flow Tuff fl'om the Ethiopian Rift Valley.
1003 *Contributions to Mineralogy and Petrology 28*, 89–111.

1004 Gibson, I.L. (1974). A review of the geology, petrology and geochemistry of the Volcano
1005 Fantale. *Bulletin of Volcanology 38*(2), 791–802.

1006 Giordano, F., D'Antonio, M., Civetta, L., Tonarini, S., Orsi, G., Ayalew, D., Yirgu, G., et al.
1007 (2014). Genesis and Evolution of Mafic and Felsic Magmas at Quaternary Volcanoes within the
1008 Main Ethiopian Rift: Insights from Gedemsa and Fanta 'Ale Complexes. *Lithos 188*, 130–144.

1009 Gleeson, M., Stock, M., Pyle, D., Mather, T., Hutchison, W., Yirgu, G. & Wade, J. (2017).
1010 Constraining Magma Storage Conditions at a Restless Volcano in the Main Ethiopian Rift Using
1011 Phase Equilibria Models. *Journal of Volcanology and Geothermal Research 337*, 44–61.

1012 Grandin, R., Socquet, A., Doin, M.P., Jacques, E., de Chabalier, J.B. & King, G.C.P. (2010).
1013 Transient rift opening in response to multiple dike injections in the Manda Hararo rift (Afar,
1014 Ethiopia) imaged by time-dependent elastic inversion of interferometric synthetic aperture radar
1015 data. *Journal of Geophysical Research 115*, B09403.

1016 Gualda, G., Ghiorso, M., Lemons, R. & Carley, T. (2012). Rhyolite-MELTS: A Modified
1017 Calibration of MELTS Optimized for Silica-Rich, Fluid-Bearing Magmatic Systems. *Journal of*
1018 *Petrology 53*, 875–890.

1019 Harris, 1844. The Highlands of Aethiopia, 2nd ed. Longman, Brown, Green and Longmans,
1020 London.

1021 Hay, E. & Wendlandt, R. (1995). The Origin of Kenya Rift Plateau-Type Phonolites: Results of
1022 High-Pressure/High-Temperature Experiments in the System Phonolite–H2O and Phonolite–
1023 H2O–CO2. *Journal of Geophysical Research 100*, 401–410.

1024 Henderson, C., & Pierozynski, W. (2012). An Experimental Study of Sr, Ba and Rb Partitioning
1025 between Alkali Feldspar and Silicate Liquid in the System Nepheline-Kalsilite-Quartz at 0.1 GPa
1026 P(H2O): A Revisitation and Reassessment. *Mineralogical Magazine 76*(1), 157–190.

1027 Hoffmann-Rothe, A., Ritter, O. & Haak, V. (2001). Magnetotelluric and Geomagnetic Modeling
1028 Reveals Zones of Very High Electrical Conductivity in the Upper Crust of Central Java. *Physics*
1029 *of the Earth and Planetary Interiors 124*, 131–151.

1030 Hübert, J., Whaler, K. & Fisseha, S. (2018). The Electrical Structure of the Central Main
1031 Ethiopian Rift as Imaged by Magnetotellurics - Implications for Magma Storage and Pathways.
1032 *Journal of Geophysical Research: Solid Earth 123*(7), 6019-6032.

1033 Huebner, J. & Dillenburg, R. (1995). Impedance Spectra of Hot, Dry Silicate Minerals and
1034 Rocks: Qualitative Interpretation of Spectra. *American Mineralogist 80*, 46–64.

1035 Humphreys, M., Blundy, J. & Sparks, S. (2008). Shallow-Level Decompression Crystallisation
1036 and Deep Magma Supply at Shiveluch Volcano. *Contributions to Mineralogy and Petrology*
1037 *155*(1), 45–61.

1038 Hutchison, W., Biggs, J., Mather, T., Pyle, D., Lewi, E., Yirgu, G., Caliro, S., et al. (2016a).
1039 Causes of Unrest at Silicic Calderas in the East African Rift: New Constraints from InSAR and
1040 Soil-Gas Chemistry at Aluto Volcano, Ethiopia. *Geochemistry, Geophysics, Geosystems 17*,
1041 3008–3030.

1042 Hutchison, W., Fusillo, R., Pyle, D., Mather, T., Blundy, J., Biggs, J., Yirgu, G., et al. (2016b) A
1043 Pulse of Mid-Pleistocene Rift Volcanism in Ethiopia at the Dawn of Modern Humans. *Nature*
1044 *Communications 7*, 13192.

1045 Hutchison, W., Mather, T., Pyle, D., Biggs, J. & Yirgu, G. (2015). Structural Controls on Fluid
1046 Pathways in an Active Rift System: A Case Study of the Aluto Volcanic Complex. *Geosphere*
1047 *11*(3), 1–21.

1048 Hutchison, W., Mather, T., Pyle, D., Boyce, A., Gleeson, M., Yirgu, G., Blundy, J., et al. (2018).
1049 The Evolution of Magma during Continental Rifting : New Constraints from the Isotopic and

Trace Element Signatures of Silicic Magmas from Ethiopian Volcanoes. *Earth and Planetary Science Letters 489*, 203–218.

Hutchison, W., Pyle, D., Mather, T., Yirgu, G., Biggs, J., Cohen, B., Barford, D., et al. (2016c). The Eruptive History and Magmatic Evolution of Aluto Volcano: New Insights into Silicic Peralkaline Volcanism in the Ethiopian Rift. *Journal of Volcanology and Geothermal Research 328*, 9–33.

Irvine, T. & Baragar, W. (1971). A Guide to the Chemical Classification of the Common Volcanic Rocks. *Canadian Journal of Earth Sciences 8*(5), 523–548.

Jackson, M., Cheadle, M. & Atherton, M. (2003). Quantitative Modelling of Granitic Melt Generation and Segregation in the Continental Crust. *Journal of Geophysical Research 108*, 2332.

Johnson, N. E., Whaler, K. A., Hautot, S., Fisseha, S., Desissa, M., & Dawes, G. J. K. (2015). Magma imaged magnetotellurically beneath an active and an inactive magmatic segment in Afar, Ethiopia. *Geological Society, London, Special Publications*, *420*, SP420-11.

Keir, D., Bastow, I., Corti, G., Mazzarini, F. & Rooney, T. (2015). The Origin of Along-Rift Variations in Faulting and Magmatism in the Ethiopian Rift. *Tectonics 34*, 464–477.

Keir, D., Ebinger, C., Stuart, G., Daly, E. & Ayele, A. (2006). Strain Accommodation by Magmatism and Faulting as Rifting Proceeds to Breakup: Seismicity of the Northern Ethiopian Rift. *Journal of Geophysical Research: Solid Earth 111*(B5).

Kidane, T., Otofuji, Y., Komatsu, Y., Shibasaki, H. & Rowland, J. (2009). Paleomagnetism of the Fentale-magmatic segment, main Ethiopian Rift: New evidence for counterclockwise block rotation linked to transtensional deformation. *Physics of the Earth and Planetary Interiors 176*, 109–123.

Komar P.D., Reimers C.E. (1978). Grain shape effects on settling rates. *The Journal of Geology* 86, 2, 193-209.

Lanzo, G., Landi, P. & Rotolo, S. (2013). Volatiles in Pantellerite Magmas: A Case Study of the Green Tuff Plinian Eruption (Island of Pantelleria, Italy). *Journal of Volcanology and Geothermal Research 262*, 153–163.

LeBas, M. J., Lemaitre, R.W., Streckeisen, A. & Zanettin, B. (1986). A Chemical Classification of Volcanic-Rocks Based on the Total Alkali Silica Diagram. *Journal of Petrology 27*(3), 745-750.

Lowenstern, J., Clynne, M. & Bullen, T. (1997). Comagmatic A-Type Granophyre and Rhyolite from the Alid Volcanic Center, Eritrea, Northeast Africa. *Journal of Petrology 38*(12) 1707–1721.

Macdonald, R. (1974) Nomenclature and Petrochemistry of the Peralkaline Oversaturated Extrusive Rocks. *Bulliten of Volcanology 38*, 498–505.

Macdonald, R. (2012) Evolution of Peralkaline Silicic Complexes: Lessons from the Extrusive Rocks. *Lithos 152*, 11–22.

1088 Macdonald, R., Baginski, B., Leat, P., White, J. & Dzierzanowski, P. (2011). Mineral Stability in
1089 Peralkaline Silicic Rocks: Information from Trachytes of the Menengai Volcano, Kenya. *Lithos*
1090 *125*, 553–568.

1091 Macdonald, R., Baginski, B., Ronga, F., Dzierzanowski, P., Lustrino, M., Marzoli, A. &
1092 Melluso, L. (2012). Evidence for Extreme Fractionation of Peralkaline Silicic Magmas, the
1093 Boseti Volcanic Complex, Main Ethiopian Rift. *Miner Petrol 104*, 163–175.

1094 Macdonald, R., Belkin, H., Fitton, J., Rogers, N., Nejbert, K., Tindle, A. & Marshall, A. (2008).
1095 The Roles of Fractional Crystallisation, Magma Mixing, Crystal Mush Remobilization and
1096 Volatile-Melt Interactions in the Genesis of a Young Basalt-Peralkaline Rhyolite Suite, the
1097 Greater OlkariaVolcanic Complex, Kenya Rift Valley. *Journal of Petrology 49*(8), 1515-1547.

1098 Macdonald, R., Navarro, J., Upton, B. & Davies, G. (1994). Strong Compositional Zonation in
1099 Peralkaline Magma: Menengai, Kenya Rift Valley. *Journal of Volcanology and Geothermal*
1100 *Research 60*, 301–325.

1101 Mahatsente, R., Jentzsch, G. & Jahr, T. (1999). Crustal structure of the Main Ethiopian Rift from
1102 gravity data: 3-dimensional modeling. *Tectonophysics 313*, 363–382.

1103 Mahood, G., & Hildreth, W. (1986). Geology of the Peralkaline Volcano at Pantelleria, Strait of
1104 Sicily. *Bulliten of Volcanology 48*(2-3), 143–172.

1105 Mahood, G. & Stimac, J. (1990). Trace-Element Partitioning in Pantellerites and Trachytes.
1106 *Geochemica et Cosmochimica Acta 54*, 2257–2276.

1107 Manzella, A., Volpi, G., Zaja, A. & Meju, M. (2004). Combined TEM-MT Investigation of
1108 Shallow-Depth Resistivity Structure of Mt Somma-Vesuvius. *Journal of Volcanology and*
1109 *Geothermal Research 131*(1), 19–32.

1110 Marshall, A., Macdonald, R., Rogers, N., Fitton, J., Tindle, A., Nejbert, K. & Hinton, R. (2009).
1111 Fractionation of Peralkaline Silicic Magmas: The Greater Olkaria Volcanic Complex, Kenya Rift
1112 Valley. *Journal of Petrology 50*(2), 323–359.

1113 Mattia, M., Bonaccorso, A. & Guglielmino, F. (2007). Ground deformations in the Island of
1114 Pantelleria (Italy): Insights into the dynamic of the current intereruptive period. *Journal of*
1115 *Geophysical Research 112*, B1406.

1116 Mazzarini, F., Corti, G., Manettie, P. & Innocenti, F. (2004). Strain Rate and Bimodal Volcanism
1117 in the Continental Rift: Debre Zeyt Volcanic Field, Northern MER, Ethiopia. *Journal of African*
1118 *Earth Sciences 39*, 415–420.

1119 McKenzie, D. (1984). The Generation and Compaction of Partially Molten Rock. *Journal of*
1120 *Petrology 25*, 713–765.

1121 Miller, D. & Smith, R. (1999). P and S Velocity Structure of the Yellowstone Volcanic Field
1122 from Local Earthquake and Controlled-Source Tomography. *Journal of Geophysical Research*
1123 *104*(B7) 15105–15121.

1124 Mohr, P. (1983). Perspectives on the Ethiopian Volcanic Province. *Bulliten of Volcanology*
1125 *46*(1), 23–43.

Mushkin, M., Stein, M., Halicz, L. & Navon, O. (2002). The Daly Gap: Low-Pressure Fractionation and Heat-Loss From Cooling Magma Chamber. *Geochemica et Cosmochimica Acta 66*(15A), A539.

Neave, D., Fabbro, G., Herd, R., Petrone, C. & Edmonds, M. (2012). Melting, Differentiation and Degassing at the Pantelleria Volcano, Italy. *Journal of Petrology 53*(3), 637–663.

Neave, D. & Putirka, K. (2017). A New Clinopyroxene-Liquid Barometer, and Implications for Magma Storage Pressures Under Icelandic Rift Zones. *American Mineralogist 102*(4), 777–794.

Nicholls, J. & Carmichael, J. (1969). Peralkaline Acid Liquids: A Petrological Study. *Contributions to Mineralogy and Petrology* 20, 268–294.

Pagli, C., Wright, T.J., Ebinger, C.J., Yun, S.H., Cann, J.R., Barnie, T.L. & Ayele, A. (2012). Shallow axial magma chamber at the slow-spreading Erta Ale Ridge. *Nature Geoscience 5*(4), 284–288.

Peccerillo, A., Barberio, M., Yirgu, G., Ayalew, D., Barbieri, M. & Wu, T. (2003). Relationships between Mafic and Peralkaline Silicic Magmatism in Continental Rift Settings: A Petrological, Geochemical and Isotopic Study of the Gedemsa Volcano, Central Ethiopian Rift. *Journal of Petrology 44*(11), 2003–2032.

Peccerillo, A., Mandefro, B., Solomon, G., Hambisa, G., Bedru, H. & Tesfaye, S. (1998). The Precambrian Rocks from Southern Ethiopia: Petrology, Geochemistry and Their Interaction with the Recent Volcanism from the Ethiopian Rift Valley. *Neues Jahrbuch Für Mineralogie-Abhandlungen*, 237–262.

Pous, J., Queralt, P., Ledo, J. & Roca, E. (1999). A High Electrical Con- Ductive Zone at Lower Crustal Depth beneath the Betic Chain (Spain). *Earth and Planetary Science Letters 167*, 35–45.

Putirka, K. (2008). Thermometers and Barometers for Volcanic Systems. In K. D. Putirka & F. J. Tepley (Eds), *Minerals, Inclusions and Volcanic Processes. Mineralogical Society of America and Geochemical Society, Reviews in Mineralogy and Geochemistry* (Vol 69, pp. 61–120).

Rabinowicz, M., Genthon, P., Ceuleneer, G. & Hillairet, M. (2001). Compaction in a Mantle Mush with High Melt Concentrations and the Generation of Magma Chambers. *Earth and Planetary Science Letters 188*, 313–328.

Rampey, M., Oppenheimer, C., Pyle, D. & Yirgu, G. (2010). Caldera-Forming Eruptions of the Quaternary Kone Volcanic Complex, Ethiopia. *Journal of African Earth Sciences 58*, 51–66.

Rampey, M., Oppenheimer, C., Pyle, D. & Yirgu, G. (2014). Physical Volcanology of the Gubisa Formation, Kone Volcanic Complex, Ethiopia. *Journal of African Earth Sciences 96*, 212–219.

Ronga, F., Lustrino, M., Marzoli, A. & Melluso, L. (2010). Petrogenesis of a Basalt-Comendite-Pantellerite Rock Suite: The Boseti Volcanic Complex (Main Ethiopian Rift). *Mineralogy and Petroogyl 98*, 227–243.

Rooney, T., Bastow, I. & Keir, D. (2011). Insights into Extensional Processes during Magma Assisted Rifting: Evidence from Aligned Scoria Cones. *Journal of Volcanology and Geothermal Research 201*(1-4), 83-96.

Rooney, T., Furman, T., Bastow, I.D., Ayalew, D. & Yirgu, G. (2007). Lithospheric modification during crustal extension in the Main Ethiopian Rift. *Journal of Geophysical Research 112*.

Rooney, T., Hart, W., Hall, C., Ayalew, D., Ghiorso, M., Hidalgo, P. & Yirgu, G. (2012). Peralkaline Magma Evolution and the Tephra Record in the Ethiopian Rift. *Contributions to Mineralogy and Petrology 164*, 407–426.

Ruprecht, P. & Bachmann, O. (2010). Pre-Eruptive Reheating during Magma Mixing at Quizapu Volcano and the Implications for the Explosiveness of Silicic Arc Volcanoes. *Geology 38*(10), 919–922.

Samrock, F., Kushinov, A., Bakker, J., Jackson, A. & Fisseha, S. (2015). 3-D Analysis and Interpretation of Magnetotelluric Data from the Aluto-Langano Geothermal Field, Ethiopia. *Geophysical Journal International 202*(3), 1923–1948.

Saria, E., Calais, E., Stamps, D., Delvaux, D. & Hartnady, C. (2014). Present-Day Kinematics of the East African Rift. *Journal of Geophysical Research: Solid Earth 119*(4), 3584–3600.

Scaillet, B., Holtz, F. & Pichavant, M. (1998). Phase Equilibrium Constraints on the Viscosity of Silicic Magmas 1. Volcanic–plutonic Comparison. *Journal of Geophysical Research 103*, 27257–27266.

Schilling, F. & Partzsch, G. (2001). Quantifying Partial Melt Portion in the Crust beneath the Central Andes and the Tibetan Plateau. *Physics and Chemistry of the Earth, Part A 26*, 239–246.

Schindelin, J., Arganda-Carreras, I., Frise, E., Kaynig, V., Longair, M., Pietzsch, T., Preibisch, S., et al. (2012). Fiji: an open-source platform for biological-image analysis, *Nature methods 9*(7), 676-682

Shand, S. (1998). On the relations between silica, alumina, and the bases in eruptive rocks, considered as a means of classification. *Geological Magazine 64*(10), 446-449.

Shirley, D. (1986). Compaction in Igneous Cumulates. *Journal of Geology 94*,795–809.

Steck, L., Thurber, C., Fehler, M., Lutter, W., Roberts, P., Baldridge, W., Stafford, D., et al. (1998). Crust and Upper Mantle P Wave Velocity Structure beneath Valles Caldera, New Mexico: Results from the Jemez Teleseismic Tomography Experiment. *Journal of Geophysical Research 103*(B10), 24301–24320.

Stevenson, R. & Wilson, L. (1997). Physical Volcanology and Eruption Dynamics of Peralkaline Agglutinates from Pantelleria. *Journal of Volcanology and Geothermal Research 79*(1-2), 97–122.

Thompson, R. & MacKenzie, W. (1990). Feldspar-Liquid Equilibria in Peralkaline Acid Liquids: An Experimental Study. *American Journal of Science 265*, 714–734.

Thy, P., Beard, J. & Lofgren, G. (1990). Experimental Constraints on the Origin of Icelandic Rhyolites. *Journal of Geology 98*, 417–421.

Trua, T., Deniel, C. & Mazzuoli, R. (1999). Crustal Control in the Genesis of Plio-Quaternary Bimodal Magmatism of the Main Ethiopian Rift (MER): Geochemical and Isotopic (Sr, Nd, Pb) Evidence. *Chemical Geology 155*, 201–231.

Tyburczy, J. & Waff, H. (1985). High Pressure Electrical Conductivity in Naturally Occurring Silicate Liquids. In R. N. Shock (Ed.), *Point Defects in Minerals, Geophysical Monograph Series* (Vol. 1, pp. 78–87). Washington, D. C.: American Geophysical Union.

Vigneresse, J., Barbey, P. & Cuney, M. (1996). Rheological Transitions During Partial Melting and Crystallisation with Application to Felsic Magma Segregation and Transfer. *Journal of Petrology 37*(6), 1579–1600.

Waff, H. & Weill, D. (1975). Electrical Conductivity of Magmatic Liquids: Effects of Temperature, Oxygen Fugacity and Composition. *Earth and Planetary Science Letters 28*, 254–260.

Wark, D., Hildreth, W., Spear, F., Cherniak, D. & Watson, E. (2007). Pre-Eruption Recharge of the Bishop Magma System. *Geology 35*(3), 235–238.

Webster, J., Taylor, R. & Bean, C. (1993). Pre-Eruptive Melt Composition and Constraints on Degassing of a Water-Rich Pantellerite Magma, Fantale Volcano, Ethiopia. *Contributions to Mineralogy and Petrology 114*, 53–62.

Whaler, K. & Hautot, S. (2006). The Electrical Resistivity Structure of the Crust beneath the Northern Main Ethiopian Rift. *Geological Society, London, Special Publications 259*, 293–305.

White, J.C., Holt, G.S., Parker, D.F. & Ren, M. (2003). Trace-element partitioning between alkali feldspar and peralkalic quartz trachyte to rhyolite magma. Part I: Systematics of trace-element partitioning. *American Mineralogist 88*, 316–329.

White, J.C., Parker, D.F. & Minghua, R. (2009). The origin of trachyte and pantellerite from Pantelleria, Italy: Insights from major element, trace element, and thermodynamic modelling. *Journal of Volcanology and Geothermal Research 179*, 33–55.

Wilks, M., Kendall, J., Nowacki, A., Biggs, J., Wookey, J., Birhanu, Y., Atalay, A., et al. (2017). Seismicity Associated with Magmatism, Faulting and Hydrothermal Circulation at Aluto Volcano, Main Ethiopian Rift. *Journal of Volcanology and Geothermal Research 340*, 52–67.

Williams, F.M., Williams, M.A.J. & Aumento, F. (2004). Tensional fissures and crustal extension rates in the northern part of the Main Ethiopian Rift. *Journal of African Earth Sciences 38*, 183–197.

WoldeGabriel, G., Aronson, J. & Walter, R. (1990). Geology, Geochronology, and Rift Basin Development in the Central Sector of the Main Ethiopia Rift. *Geological Society of America Bulletin 102*, 439–458.

Wotzlaw, J., Bindeman, I., Watts, K., Schmitt, A., Caricchi, L. & Schaltegger, U. (2014). Linking Rapid Magma Reservoir Assembly and Eruption Trigger Mechanisms at Evolved Yellowstone-Type Supervolcanoes. *Geology 42*(9), 807–810.

Xu, W., Rivalta, E. & Ling, X. (2017). Magmatic architecture within a rift segment: Articulate axial magma storage at Erta Ale volcano, Ethiopia. *Earth and Planetary Science Letters 476*, 79–86.

Zandt, G., Leidig, M., Chmielowski, J., Baumont, D. & Yuan, X. (2003). Seismic Detection and Characterization of the Altiplano-Puna Magma Body, Central Andes. *Pure and Applied Geophysics 160*(3-4), 789–807.

1243 **Table 1:** Selected whole-rock data for Kone and Fentale volcanoes acquired via XRF analysis at the Department of Geology at the University of Leicester. LOI=
1244 loss on ignition; bdl = below detection limit; A.I. = agpaitic index (molar $(Na_2O+K_2O)/Al_2O_3$).

1245

Sample		Kone3.9	Kone3.18	Kone3.30	Kone3.41	Kone4.10	K04	K05	K06	K07	KoneBG25	KoneBN29	MER128A	MER130A	MER133A
Rock Type		Pumice airfall	Pumice airfall	Porphyritic obsidian	Pumice airfall	Porphyritic obsidian	Porphyritic obsidian	Ignimbrite	Pumice lapilli	Porphyritic obsidian	Porphyritic obsidian	Welded ignimbrite	Pumice lapilli breccia	Pumice lapilli breccia	Basalt scoria
Relative Age		Kone caldera	Kone caldera	Post-Kone caldera	Kone caldera	Pre-Kone caldera	Pre-Birenti caldera	Birenti caldera	Post-Kone caldera	Post-Kone caldera	Pre-Kone caldera	Kone caldera	Kone caldera	Kone caldera	Post-Kone caldera
Location	Lat. (N)	8.8178	8.8280	8.8691	8.8244	8.8628	8.7875	8.7875	8.8156	8.8158	Northwest rim of Kone caldera	South wall Kone caldera	8.7877	8.8091	8.8544
	Long. (E)	39.6769	39.6538	39.7250	39.6591	39.6640	39.7383	39.7383	39.6995	39.7008			39.6589	39.6873	39.7469
SiO_2	wt%	66.20	66.73	70.01	72.01	70.15	70.14	70.28	72.69	71.64	70.73	66.71	65.24	69.36	46.40
TiO_2	wt%	0.40	0.29	0.46	0.23	0.39	0.46	0.48	0.21	0.23	0.39	0.47	0.51	0.23	1.99
Al_2O_3	wt%	10.90	7.45	9.30	10.27	7.93	9.32	10.18	8.11	8.42	7.89	11.39	8.95	8.40	15.14
FeO_T	wt%	6.56	8.52	8.34	4.54	9.16	7.92	8.27	8.57	7.97	8.98	7.00	7.67	6.28	12.04
MnO	wt%	0.24	0.29	0.28	0.14	0.30	0.30	0.30	0.31	0.29	0.33	0.30	0.30	0.23	0.18
MgO	wt%	0.06	0.08	0.03	0.08	0.04	0.02	0.11	0.07	0.07	0.04	0.09	0.28	0.16	8.42
CaO	wt%	0.45	0.38	0.38	0.28	0.38	0.41	0.88	0.60	0.34	0.36	0.59	1.80	0.62	10.15
Na_2O	wt%	4.57	6.43	6.39	4.63	6.67	6.49	5.64	3.12	6.76	6.68	6.05	3.63	3.90	2.84
K_2O	wt%	4.95	4.69	4.40	4.94	4.32	4.37	4.08	5.65	4.16	4.29	4.64	5.09	5.52	0.85
P_2O_5	wt%	0.03	0.03	0.03	0.02	0.03	0.02	0.03	0.02	0.02	0.02	0.04	0.03	0.02	0.51
LOI	wt%	3.44	3.48	-0.27	2.26	-0.36	-0.01	0.06	0.24	-0.01	-0.34	2.18	5.44	4.28	0.25
Total	wt%	99.17	98.38	98.85	99.40	99.03	99.45	100.29	99.59	99.90	99.39	99.48	98.98	99.02	98.77
A.I.		1.18	2.10	1.64	1.26	1.97	1.65	1.35	1.39	1.86	1.98	1.32	1.28	1.47	0.37
Ba	ppm	176.7	95.6	53.1	39.2	79.0	64.6	146.7	248.8	220.6	83.6	591.6	65.5	30.4	395.5
Ce	ppm	214.3	275.7	206.8	203.4	295.7	220.9	246.0	334.7	274.6	329.0	192.1	208.0	471.1	52.0
Co	ppm	2.4	3.7	5.2	1.5	4.3	3.6	1.5	3.4	2.6	4.7	5.0	4.8	5.0	51.7
Cr	ppm	bdl	bdl	bdl	bdl	bdl	bdl	bdl	bdl	bdl	bdl	bdl	bdl	bdl	326.1
La	ppm	102.2	120.9	100.9	97.1	139.7	110.5	125.2	166.5	135.4	153.8	92.9	99.0	227.6	22.6
Nb	ppm	156.0	209.7	143.0	132.6	223.6	145.1	158.2	215.0	179.3	228.5	125.7	127.6	325.8	29.6
Ni	ppm	bdl	bdl	bdl	bdl	bdl	bdl	bdl	bdl	bdl	bdl	bdl	2.1	5.6	121.1
Rb	ppm	124.6	162.2	142.7	178.6	168.5	145.4	132.9	220.1	161.2	173.6	102.7	131.1	332.2	14.7
Sr	ppm	5.3	11.5	3.8	10.0	6.4	0.60	23.8	37.9	6.1	6.0	10.8	81.0	27.4	427.1
Th	ppm	16.9	21.1	18.2	20.2	23.5	18.0	18.3	25.7	20.7	23.6	13.6	14.8	45.3	1.9
Y	ppm	118.9	170.1	117.5	99.1	175.4	120.1	84.4	188.1	152.5	179.6	100.9	110.5	243.3	30.4
Zr	ppm	1029.7	1324.6	947.0	882.1	1411.6	1006.2	1077.4	1486.2	1215.9	1447.9	832.9	836.8	2141.9	152.0

Sample		MER136A	MER137A	MER138A	MER140Bb	F01	F03	F12	F16	F27	F41	F44	F48	F49
Rock Type		Basalt scoria	Basalt scoria	Basalt scoria	Welded ignimbrite	Porphyritic obsidian	Pumice lapilli	Basaltic scoria	Porphyritic obsidian	Porphyritic obsidian	Pumice lapilli	Welded ignimbrite	Welded ignimbrite	Basalt scoria
Relative Age		Post-Kone caldera	Post-Kone caldera	Post-Kone caldera	Kone caldera	Pre-caldera	Pre-caldera	Post-caldera	Post-caldera	Pre-caldera	Post-caldera	Caldera	Caldera	Post-caldera
Location	Lat. (N)	8.8239	8.8292	8.8418	8.8434	8.9978	8.9978	8.9381	8.9584	8.9776	8.9578	8.9577	8.9279	8.9525
	Long. (E)	39.7047	39.7096	39.7139	39.7332	39.8709	39.8709	39.8927	39.9271	39.8733	39.8992	39.8986	39.8432	39.7550
SiO_2	wt%	46.48	46.32	46.25	72.07	69.56	70.11	46.94	71.65	69.63	71.76	69.24	69.98	46.45
TiO_2	wt%	2.23	2.17	2.29	0.37	0.52	0.50	3.92	0.38	0.48	0.35	0.51	0.42	2.44
Al_2O_3	wt%	14.65	14.54	14.71	10.09	9.59	9.32	13.62	9.41	8.23	8.99	9.83	9.15	15.58
FeO_T	wt%	12.60	12.54	12.60	6.34	8.42	8.36	15.51	7.40	9.40	7.45	8.65	8.47	13.03
MnO	wt%	0.19	0.19	0.19	0.22	0.36	0.33	0.28	0.28	0.40	0.28	0.33	0.33	0.18
MgO	wt%	8.81	9.23	8.58	0.10	0.02	0.07	4.78	0.20	0.05	0.06	0.18	0.11	8.26
CaO	wt%	10.55	10.51	10.68	0.37	0.47	0.86	9.04	0.81	0.41	0.41	0.72	0.54	10.44
Na_2O	wt%	3.10	2.93	3.09	5.49	6.82	5.44	3.96	6.29	6.83	5.83	6.50	6.40	2.95
K_2O	wt%	0.97	0.92	0.99	4.43	4.13	4.54	0.89	3.80	4.19	4.21	3.99	4.26	0.73
P_2O_5	wt%	0.52	0.48	0.55	0.03	0.03	0.03	1.18	0.07	0.03	0.02	0.05	0.03	0.45
LOI	wt%	-0.55	-0.36	-0.32	0.18	-0.02	0.18	-0.03	-0.01	-0.02	0.13	0.07	0.13	0.50
Total	wt%	99.58	99.50	99.61	99.67	99.91	99.75	100.20	100.28	99.69	99.55	100.07	99.86	101.01
A.I.		0.42	0.40	0.42	1.37	1.64	1.49	0.55	1.54	1.92	1.57	1.53	1.65	0.36
Ba	ppm	391.3	364.6	425.7	208.6	637.2	702.0	474.2	269.2	769.9	422.5	614.0	530.2	274.6
Ce	ppm	62.8	59.0	63.4	275.9	240.6	259.7	68.2	319.5	266.1	320.8	239.7	255.7	46.3
Co	ppm	51.5	52.9	48.9	4.2	3.8	2.0	27.2	3.3	3.0	4.2	2.1	2.9	48.1
Cr	ppm	386.1	435.7	351.5	bdl	bdl	bdl	6.7	bdl	bdl	bdl	bdl	bdl	219.5
La	ppm	32.1	24.7	31.0	127.5	119.3	130.2	30.1	160.4	132.2	158.1	116.3	127.8	20.6
Nb	ppm	39.4	36.5	41.6	192.1	159.6	164.9	36.5	226.6	174.8	208.2	156.2	166.6	26.6
Ni	ppm	137.4	157.4	123.3	bdl	bdl	bdl	bdl	bdl	bdl	bdl	bdl	bdl	56.2
Rb	ppm	25.1	22.8	25.6	167.4	119.5	128.1	18.7	162.0	123.1	153.1	117.5	128.3	13.9
Sr	ppm	577.2	551.8	596.7	15.5	7.3	37.6	502.1	43.7	12.8	12.1	27.5	18.9	507.0
Th	ppm	2.8	2.9	3.4	23.7	15.4	15.8	23.0	23.0	15.2	20.6	15.3	16.3	1.5
Y	ppm	27.5	26.6	28.6	125.5	133.4	143.6	44.3	169.3	153.2	175.1	128.2	140.9	25.2
Zr	ppm	161.8	151.6	167.0	1240.3	1020.1	1057.3	168.3	1431.9	1092.9	1391.0	1023.6	1100.5	142.9

1246 **Table 2:** Selected glass data for Aluto, Kone, and Fentale volcanoes. Major elements were acquired via EPMA at the Department of Earth Sciences at the
1247 University of Cambridge, trace elements were acquired via SIMS at the School of Geosciences at the University of Edinburgh. bdl = below detection limit; A.I. =
1248 agpaitic index (molar $(Na_2O+K_2O)/Al_2O_3$).

Sample		01-02-24	13-05-04	26-01-SMP	31-01-LE	F01	F11	F16	F17	F27	F42	F44	F48	K3.9	K3.18
Rock type		Porphyritic obsidian	Welded ignimbrite	Porphyritic obsidian	Porphyritic obsidian	Porphyritic obsidian	Welded ignimbrite	Porphyritic obsidian	Pumice lapilli	Porphyritic obsidian	Pumice lapilli	Welded ignimbrite	Welded ignimbrite	Pumice lapilli	Pumice lapilli
Relative age		Post-caldera	Caldera	Post-caldera	Post-caldera	Pre-caldera	Caldera	Post-caldera	Post-caldera	Pre-caldera	Post-caldera	Caldera	Caldera	Kone caldera	Kone caldera
Location	Lat. (N)	7.7698	7.8407	7.8161	7.7832	8.9978	8.9378	8.9584	8.9535	8.9776	8.9578	8.9577	8.9279	8.8178	8.8280
	Long. (E)	38.7471	38.7303	38.7773	38.8268	39.8709	39.8934	39.9271	39.9295	39.8733	39.8992	39.8986	39.8432	39.6769	39.6538
SiO_2	wt%	74.16	73.02	73.36	74.02	70.67	69.78	70.37	72.65	70.54	73.12	71.42	70.34	74.97	75.15
TiO_2	wt%	0.28	0.31	0.16	0.26	0.55	0.49	0.20	0.51	0.54	0.53	0.42	0.31	0.14	0.15
Al_2O_3	wt%	10.16	9.20	8.95	9.09	9.58	9.48	11.98	8.87	9.48	9.11	8.76	11.20	8.68	8.79
FeO	wt%	5.33	6.49	6.86	6.27	8.03	8.69	5.31	7.60	8.09	7.54	8.22	6.23	6.12	6.19
MnO	wt%	0.27	0.26	0.38	0.33	0.43	0.39	0.23	0.36	0.41	0.35	0.39	0.29	0.32	0.32
MgO	wt%	bdl	0.02	bdl	bdl	0.02	0.01	0.03	0.01	0.01	bdl	0.02	0.02	0.02	bdl
CaO	wt%	0.20	0.19	0.20	0.23	0.28	0.52	0.15	0.41	0.33	0.37	0.35	0.21	0.19	0.20
Na_2O	wt%	5.11	4.87	5.66	5.22	5.71	6.10	6.35	5.24	5.88	4.67	5.89	6.20	5.20	4.79
K_2O	wt%	4.50	5.65	4.42	4.53	4.60	4.39	5.33	4.32	4.63	4.31	4.48	5.11	4.36	4.39
P_2O_5	wt%	bdl	bdl	0.02	0.05	0.13	0.16	0.04	0.02	0.10	bdl	0.07	0.06	bdl	0.03
A.I.		1.31	1.54	1.57	1.49	1.50	1.56	1.35	1.50	1.55	1.36	1.66	1.40	1.10	1.05
Ba	ppm	367.2	107.9	393.4	370.5	694.2	679.5	292.3	853.3	856.9	482.1	652.6	525.7	247.3	246.0
Ce	ppm	198.9	290.7	324.8	267.1	210.2	190.4	323.8	270.0	236.3	299.5	200.5	239.0	357.3	347.8
La	ppm	98.5	149.4	162.1	134.1	104.9	91.6	166.5	136.8	117.9	151.3	99.2	122.7	177.6	172.4
Nb	ppm	132.9	240.5	212.8	177.8	152.5	124.6	258.5	179.2	163.1	212.8	137.3	165.3	230.1	230.3
Rb	ppm	101.1	117.7	147.9	126.6	118.9	17.1	198.7	141.2	126.5	168.8	114.3	128.6	147.3	146.2
Sr	ppm	4.7	4.3	6.8	5.8	8.3	9.5	14.6	10.9	13.2	12.5	10.0	9.7	4.5	4.3
Y	ppm	97.8	120.0	158.8	130.3	121.9	102.4	186.0	147.1	140.1	169.6	115.4	140.3	157.0	154.0
Zr	ppm	814.2	1387.5	1319.4	1085.7	890.0	780.1	1495.6	1019.4	952.6	1304.9	816.8	1007.1	1362.1	1371.0

1249

Sample		K3.30	K3.41	K4.10	K06	KBG25	KBN29	M057A	MER128A	M130A	MER133A	MER136A	MER137A	MER138A	MER140Bb
Rock type		Porphyritic obsidian	Pumice airfall	Porphyritic obsidian	Pumice lapilli	Porphyritic obsidian	Welded ignimbrite	Pumice lapilli	Pumice lapilli breccia	Pumice lapilli breccia	Basalt scoria	Basalt scoria	Basalt scoria	Basalt scoria	Welded ignimbrite
Relative age		Post-Kone caldera	Kone caldera	Pre-Kone caldera	Post-Kone caldera	Pre-Kone caldera	Kone caldera	Post-caldera	Kone caldera	Kone caldera	Post-Kone caldera	Post-Kone caldera	Post-Kone caldera	Post-Kone caldera	Kone caldera
Location	Lat. (N)	8.8691	8.8244	8.8628	8.8156	8.8000	8.8000	7.7865	8.7877	8.8091	8.8544	8.8239	8.8292	8.8418	8.8434
	Long. (E)	39.7250	39.6591	39.6640	39.6995	39.6920	39.6920	38.8098	39.6589	39.6873	39.7469	39.7047	39.7096	39.7139	39.7332
SiO_2	wt%	70.53	75.22	71.36	72.91	70.75	70.43	75.37	75.55	75.45	48.95	47.40	47.69	47.56	73.17
TiO_2	wt%	0.49	0.18	0.39	0.22	0.35	0.48	0.30	0.19	0.18	2.54	3.14	2.72	2.94	0.24
Al_2O_3	wt%	10.39	9.65	8.58	7.89	9.86	10.97	8.75	9.24	8.78	14.39	14.68	15.83	15.09	9.05
FeO	wt%	7.41	5.11	8.50	7.78	7.50	7.26	6.14	5.91	6.01	11.84	12.73	11.88	12.39	6.46
MnO	wt%	0.31	0.18	0.36	0.32	0.35	0.33	0.30	0.26	0.32	0.18	0.26	0.24	0.24	0.25
MgO	wt%	bdl	bdl	0.03	0.01	0.03	0.04	bdl	bdl	bdl	6.71	5.14	5.00	4.98	0.02
CaO	wt%	0.37	0.19	0.37	0.25	0.33	0.40	0.20	0.21	0.19	11.35	10.48	10.60	10.60	0.21
Na_2O	wt%	5.89	5.03	5.95	6.23	6.11	5.31	4.75	4.42	4.73	2.45	3.90	4.04	4.01	5.61
K_2O	wt%	4.55	4.44	4.42	4.39	4.66	4.65	4.20	4.23	4.32	0.99	1.51	1.39	1.44	4.91
P_2O_5	wt%	0.06	bdl	0.05	bdl	0.06	0.12	bdl	bdl	0.02	0.61	0.76	0.62	0.76	0.08
A.I.		1.01	0.98	1.21	1.35	1.09	0.91	1.41	0.94	1.03	0.24	0.37	0.34	0.36	1.16
Ba	ppm	72.5	24.8	96.8	298.9	95.7	455.7	245.2	153.1	215.1	447.2	513.8	467.1	513.7	59.9
Ce	ppm	181.7	255.9	268.8	316.2	268.5	203.5	298.6	318.7	196.1	64.5	91.6	79.1	86.4	290.7
La	ppm	91.4	131.8	136.3	159.4	134.4	102.7	147.2	160.5	97.2	29.1	44.3	40.3	43.1	149.0
Nb	ppm	130.3	202.7	209.1	216.6	207.5	148.7	200.3	229.3	130.8	32.6	53.0	43.9	49.8	225.3
Rb	ppm	156.5	261.9	192.3	214.3	194.8	152.1	151.4	240.0	89.0	22.8	38.7	32.2	36.4	245.1
Sr	ppm	2.2	5.1	4.7	8.5	4.7	4.9	4.5	4.2	3.3	580.4	590.0	625.6	624.8	2.7
Y	ppm	102.1	138.8	158.3	175.2	158.2	104.3	132.8	154.0	91.0	30.4	37.1	30.8	34.6	159.5
Zr	ppm	828.2	1202.1	1296.4	1353.9	1287.8	903.4	1131.9	1374.3	768.6	158.1	224.0	191.5	210.7	1395.3

Sample	n	XAn, XAb, XOr	Concentration (ppm)				Partition Coefficients	
			Ba mean	Ba min	Ba max	Ba σ	D_{Ba}	σ
Plagioclase								
13-05-04	1	An(37-42), Ab(60-56), Or(3-3)	2002	1691	2313	440	N/A	N/A
18-11-07	45	An(5-39), Ab(77-58), Or(3-24)	2875	920	4061	775	N/A	N/A
MER140Bb	3	An(11-20), Ab(73-72), Or(8-18)	3439	3114	3745	316	N/A	N/A
Alkali feldspar								
31-01-LE	6	An(0.1-0.4), Ab(65-58), Or(35-65)	1216	676	2443	496	3.56	1.52
26-01-SMP	10	An(0.1-0.3), Ab(60-50), Or(40-50)	800	489	2230	290	2.16	0.44
13-05-04	12	An(0.1-3), Ab(68-57), Or(32-43)	466	182	2350	421	6.37	5.12
F01	7	An(0.2-0.5), Ab(71-69), Or(28-31)	1535	1218	1987	267	2.35	0.33
F16	7	An(0.1-0.2), Ab(63-55), Or(37-45)	562	244	872	190	2.07	0.68
F27	15	An(0.1-0.5), Ab(71-66), Or(28-33)	1196	769	2681	303	1.39	0.35
F44	12	An(0.1-2), Ab(76-61), Or(24-39)	1467	405	4064	853	2.80	1.4
F48	6	An(0.1-1), Ab(73-63), Or(26-37)	1041	347	2061	653	2.83	1.2
K04	2	An(0.3-0.3), Ab(70-68), Or(30-32)	575	420	728	160	N/A	N/A
K05	3	An(0.1-0.3), Ab(68-66), Or(30-34)	443	309	778	155	N/A	N/A
KBN29	21	An(0.2-3), Ab(71-64), Or(29-35)	1477	835	2790	410	3.06	0.92
M057A	3	An(0.1-0.4), Ab(62-54), Or(38-46)	680	510	923	149	3.24	0.47
M140Bb	2	An(0.1-0.1), Ab(66-60), Or(34-40)	637	331	1044	340	9.35	5.41

Table 3: Selected feldspar data for Aluto, Kone, and Fentale volcanoes acquired via EPMA at the Department of Earth Sciences at the University of Cambridge. Partition coefficients given are the average 'apparent' partition coefficients calculated from feldspar rim and corresponding glass compositions. n = number of crystals analysed (typically one analysis of plagioclase crystals, two analyses representing core and rim sections of the crystal for alkali feldspars) ; X_{An} = anorthoclase content; X_{Ab} = albite content; X_{Or} = orthoclase content; N/A = partition coefficients not calculated (due to lack of glass and/or feldspar rim compositions).

Figure 1: a) Map locating the Main Ethiopian Rift **(b)** within the larger eastern branch of the East African Rift system. Peralkaline calderas are outlined in dark blue, with Quaternary eruption deposits highlighted in white (Corti, 2008). The red lines represent the Wonji Fault Belt, where the majority of extensional stress is accommodated; the black lines represent the older, less active border faults (Corti, 2008). Aluto volcano is located at the southern end of the central Main Ethiopian Rift, Kone and Fentale are located at the northern end; simplified geological maps (adapted from Hutchison et al., 2016c; Rampey et al., 2010; Gibson, 1974) are shown for both **(c, d and e, respectively)**.

Figure 2: QEMSCAN phase assemblage maps showing key petrological textures. The QEMSCAN software creates phase assemblage maps from data acquired from a combination of low-count energy-dispersive X-ray spectra (EDX) and BSE brightness and X-ray count information. From top left to bottom right- a) Fe chemical map displaying the phase assemblage and petrological textures of a post-caldera basaltic scoria from Kone. Note the glomerocrystic clotting of phenocrysts, and zoned olivines (red) and clinopyroxene (green); b) Crystal-rich trachytic ignimbrite from Aluto, dominated by anorthoclase. Some crystals are normally zoned with plagioclase cores. Fayalite, aegirine augite, and microphenocrysts of Fe-Ti oxides form glomerocrystic clots with the feldspar. Quartz completes the assemblage; all is set in a devitrified groundmass; c) Crystal-rich rhyolitic ignimbrite from Kone,

showing a large fiamme on the right. Dominated by anorthoclase, quartz, aegirine-augite and aenigmatite complete the phase assemblage, all set in a devitrified groundmass; d) Pumice lapillus from a fall deposit from Kone associated with the caldera formation. The phase assemblage present is similar to related ignimbrites, dominated by anorthoclase. Aegirine augite and microphenocrysts of Fe-Ti oxides form glomerocrystic clots to give a similar texture; e) Trachytic pre-caldera lava from Kone, dominated by anorthoclase. Aegirine augite and Fe-Ti oxides are also present, forming glomerocrystic clots with the feldspar crystals. The fine-medium groundmass is dominated by quartz, alkali feldspar and aegirine augite; f) A comparatively more crystal-poor rhyolitic lava from Aluto. The phase assemblage is dominated by anorthoclase, aenigmatite and aegirine augite. Complex granophyric intergrowths of alkali feldspar and quartz are common.

Figure 3: Whole-rock analyses of Kone and Fentale samples. Dashed fields show Aluto data coverage (Hutchison et al., 2016c), glass analyses for the three volcanoes are shown by unfilled symbols- **a)** Total alkalis versus silica (TAS) diagram. The dashed line shows the alkaline-sub-alkaline divide of Irvine and Baragar (1971); **b)** Classification diagram of peralkaline rhyolites and trachytes (Macdonald, 1974). Colours are used to denote the three different volcanoes throughout the paper, shapes the relative age of deposits. Errors are smaller than symbols shown.

Figure 4: Harker variation diagrams of whole-rock and glass major element compositions. Dashed fields show Aluto whole-rock data coverage (Hutchison et al., 2016c), solid lines show melt composition predicted by the best-fit RhyoliteMELTS models (Gleeson et al., 2017; Gualda et al., 2012). Errors are smaller than symbols shown.

Figure 5: Whole-rock and glass trace element compositions plotted against Zr concentration due to its incompatibility **(a)**. Dashed fields show Aluto whole-rock data coverage (Hutchison et al., 2016c), shaded field shows Precambrian crustal rock geochemistry (Peccerillo et al., 1998), which likely represent a component of the basement rocks. Key as in **figure 3**. Errors are smaller than symbols shown.

Figure 6: Feldspar classification ternary diagram, solid lines show feldspar compositions predicted by the best-fit RhyoliteMELTS models (Gleeson et al., 2017; Gualda et al., 2012).

Figure 7: Feldspar trace element compositions are highly variable, to investigate the presence/absence of zoning plot a) shows Ba and Or concentration in the core of the alkali felspar normalised by the concentration of Ba and Or in the rim, whilst b) shows selected Ba profiles across a number of crystals from Kone, Fentale and Aluto. Key as in **figure 6**.

Figure 8: Melt SiO_2 predicted by best-fit RhyoliteMELTS models (Gualda et al., 2012) for Kone and Fentale volcanoes against **(a)** the predicted melt temperature, **(b)** the predicted liquid fraction (F), and **(c)** the relative rates of differentiation (change in silica content with respect to time), estimated from RhyoliteMELTS output at wall rock temperatures of 500 °C (solid lines) and 700 °C (dashed lines).

Figure 9: Plot showing observed feldspar Ba contents against observed glass Ba contents. Partition coefficients calculated based on the experimental work of Henderson and Pierozynski (2012) have been used to predict glass Ba concentrations based on feldspar rim compositions (solid lines). Dashed lines show where adjusted values of NKA have been used in the calculation due to probable Na_2O loss. Melt Ba contents based on the observed partition coefficients of Mahood and Stimac (1990) are also indicated by the thick solid lines. Errors in feldspar Ba content are displayed by horizontal lines, errors in glass Ba content were smaller than the symbols shown.

Figure 10: Plots showing **(a)** feldspar and **(b)** glass Ba concentrations against glass SiO_2. 'Apparent' feldspar-melt Ba partition coefficients are shown against glass SiO_2 **(c)** and NKA **(d)**. Solid lines depict the result of models based on the liquid line of descent from best-fit RhyoliteMELTS models (Gleeson et al., 2017; Gualda et al., 2012) in tandem with a parameterisation of the feldspar-melt partition coefficient based on peralkalininity and temperature (after Henderson & Pierozynski, 2012). Thick black lines **(c and d)** represent the minimum and maximum observed partition coefficients presented by Mahood and Stimac (1990). Experimental data from Henderson and Pierozynski (2012) is also plotted, along with observed values from Mahood and Stimac (1990).

Figure 11: Schematic showing the hypothesised structure of peralkaline magma reservoirs beneath MER volcanoes. Peralkaline magmas are fed by a mafic melts that undergo protracted fractional crystallisation. The shallow reservoir is dominated by a feldspar-rich mush, built up by crystal-melt segregation, aided by the low-viscosity of peralkaline melts. Feldspar crystallisation steadily strips the residual melts of compatible trace elements, such as Ba, leading to a compositional stratification of the mush pile. During explosive caldera-forming eruptions crystals are scavenged from deep in this mush pile, leading to the incorporation of feldspar crystals that are too Ba-enriched to be in equilibrium with their carrier melts. Post-caldera eruptions primarily tap residual melt lenses and do not appear to incorporate significant portions of crystal mush.

Figure 12: Plot showing the time required to segregate 0.01 km^3 of crystal poor pantellerite (black lines) and metaluminous rhyolite (grey lines) from crystals by compaction (solid lines) and hindered settling (dashed lines) as a function of the grain size. An example crystal size distribution for a typical Aluto pantellerite post-caldera lava is shown above.

Figure 1.

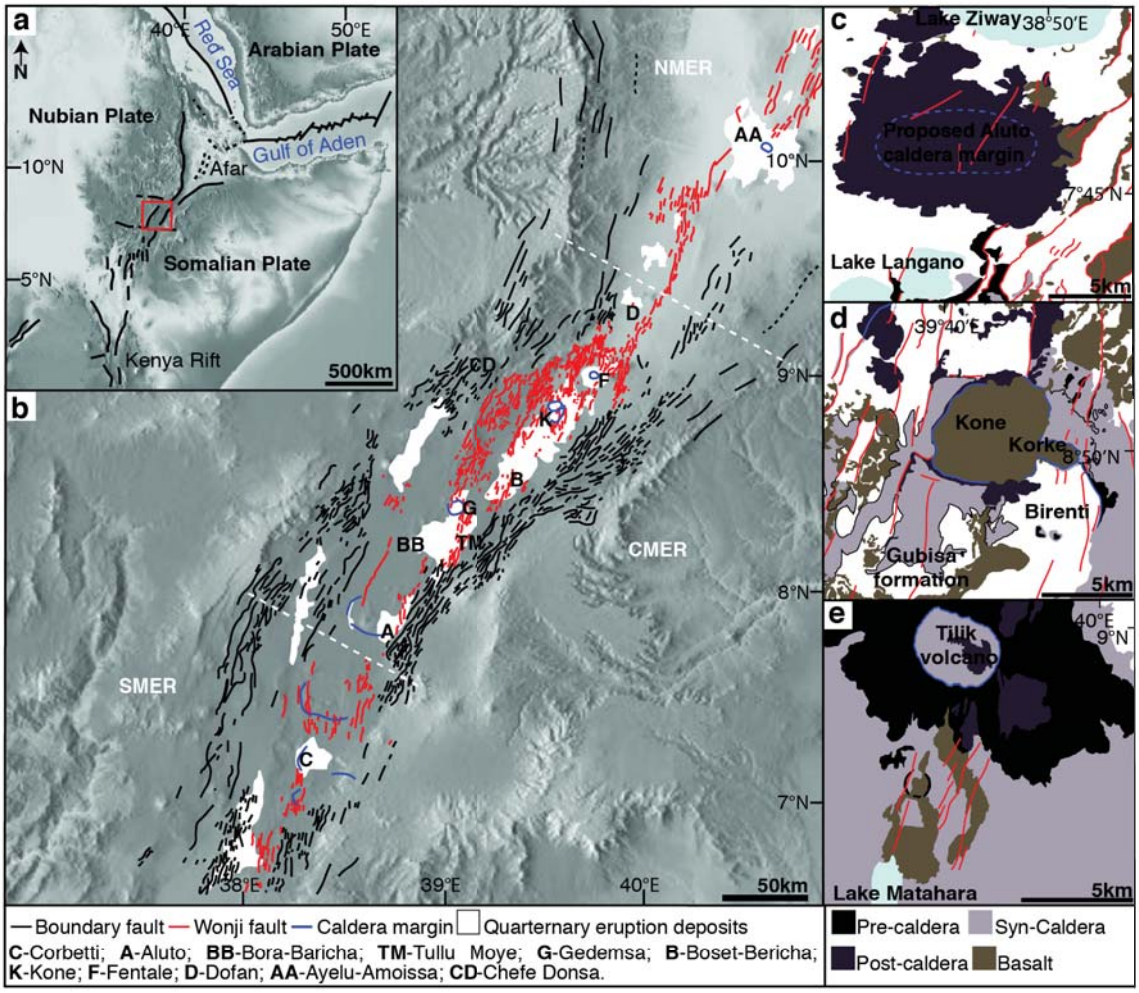
a
40°E
50°E
N
Red Sea
Arabian Plate
Nubian Plate
Gulf of Aden
10°N
Afar
Somalian Plate
5°N
Kenya Rift
500km
b
NMER
AA
10°N
D
CD
F
9°N
K
B
G
BB
TM
CMER
8°N
A
SMER
C
7°N
38°E
39°E
40°E
50km
c
Lake Ziway
38°50'E
Proposed Aluto caldera margin
7°45'N
Lake Langano
5km
d
39°40'E
Kone
Korke
8°50'N
Birenti
Gubisa formation
5km
e
40°E
9°N
Tilik volcano
Lake Matahara
5km
— Boundary fault — Wonji fault — Caldera margin Quarternary eruption deposits
C-Corbetti; A-Aluto; BB-Bora-Baricha; TM-Tullu Moye; G-Gedemsa; B-Boset-Bericha; K-Kone; F-Fentale; D-Dofan; AA-Ayelu-Amoissa; CD-Chefe Donsa.
Pre-caldera
Syn-Caldera
Post-caldera
Basalt

Figure 2.

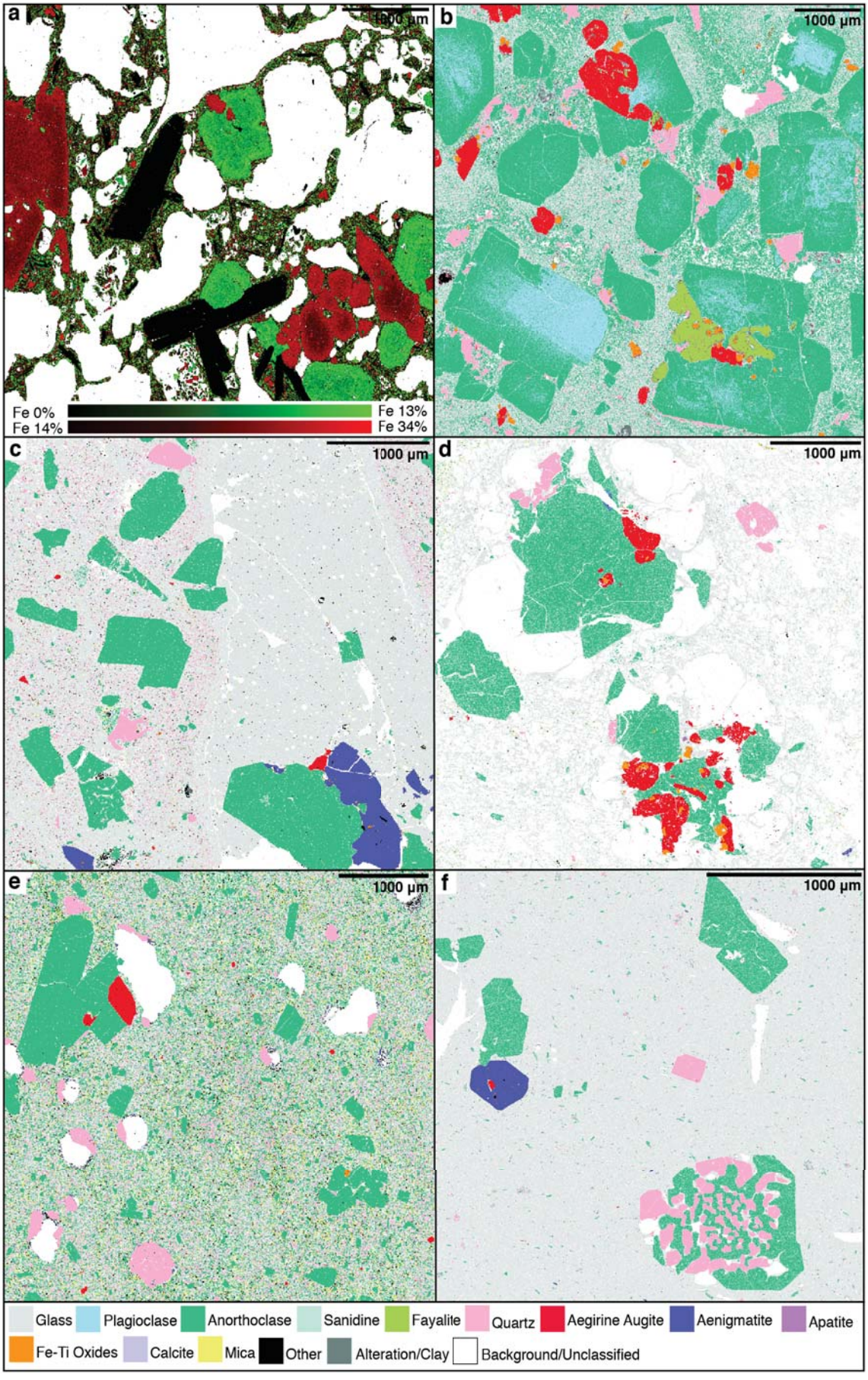
a
1000 µm
Fe 0%
Fe 14%
Fe 13%
Fe 34%
b
1000 µm
c
1000 µm
d
1000 µm
e
1000 µm
f
1000 µm
Glass
Plagioclase
Anorthoclase
Sanidine
Fayalite
Quartz
Aegirine Augite
Aenigmatite
Apatite
Fe-Ti Oxides
Calcite
Mica
Other
Alteration/Clay
Background/Unclassified

Figure 3.

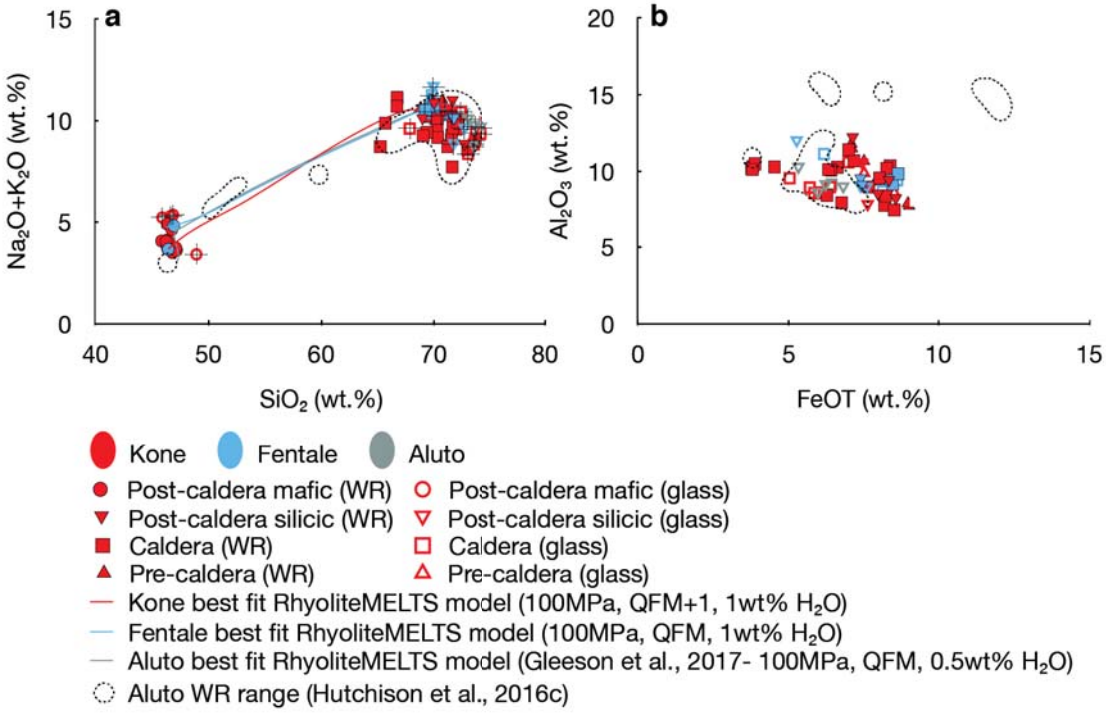
a
b
15
10
5
0
40
50
60
70
80
Na_2O+K_2O (wt.%)
SiO_2 (wt.%)
20
15
10
5
0
0
5
10
15
Al_2O_3 (wt.%)
FeOT (wt.%)
Kone
Fentale
Aluto
Post-caldera mafic (WR)
Post-caldera silicic (WR)
Caldera (WR)
Pre-caldera (WR)
Post-caldera mafic (glass)
Post-caldera silicic (glass)
Caldera (glass)
Pre-caldera (glass)
Kone best fit RhyoliteMELTS model (100MPa, QFM+1, 1wt% H_2O)
Fentale best fit RhyoliteMELTS model (100MPa, QFM, 1wt% H_2O)
Aluto best fit RhyoliteMELTS model (Gleeson et al., 2017- 100MPa, QFM, 0.5wt% H_2O)
Aluto WR range (Hutchison et al., 2016c)

Figure 4.

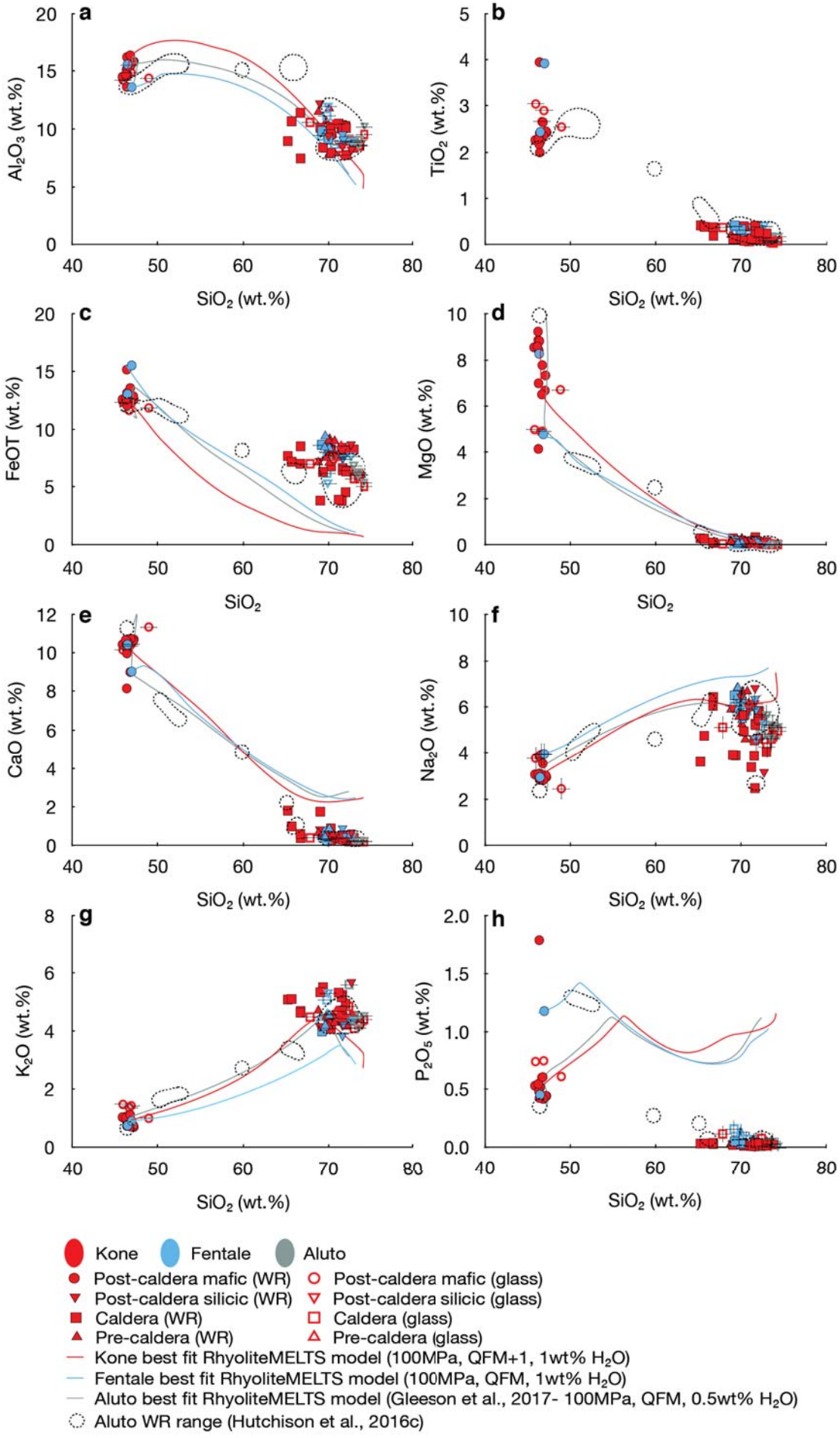
a
b
c
d
e
f
g
h
Al2O3 (wt.%)
TiO2 (wt.%)
FeOT (wt.%)
MgO (wt.%)
CaO (wt.%)
Na2O (wt.%)
K2O (wt.%)
P2O5 (wt.%)
SiO2 (wt.%)
SiO2
Kone
Fentale
Aluto
Post-caldera mafic (WR)
Post-caldera silicic (WR)
Caldera (WR)
Pre-caldera (WR)
Post-caldera mafic (glass)
Post-caldera silicic (glass)
Caldera (glass)
Pre-caldera (glass)
Kone best fit RhyoliteMELTS model (100MPa, QFM+1, 1wt% H2O)
Fentale best fit RhyoliteMELTS model (100MPa, QFM, 1wt% H2O)
Aluto best fit RhyoliteMELTS model (Gleeson et al., 2017- 100MPa, QFM, 0.5wt% H2O)
Aluto WR range (Hutchison et al., 2016c)

Figure 5.

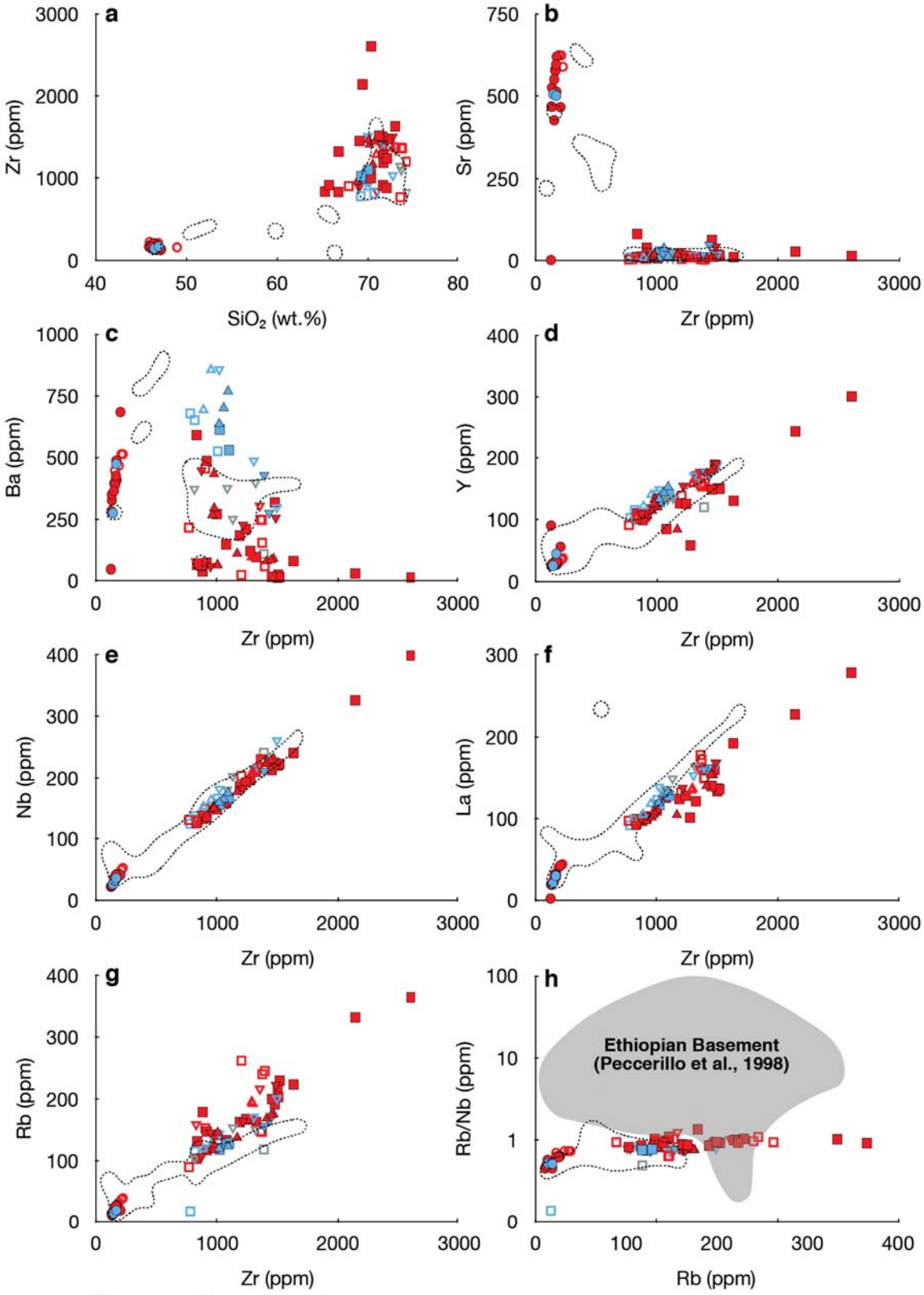
a
Zr (ppm)
SiO2 (wt.%)
b
Sr (ppm)
Zr (ppm)
c
Ba (ppm)
Zr (ppm)
d
Y (ppm)
Zr (ppm)
e
Nb (ppm)
Zr (ppm)
f
La (ppm)
Zr (ppm)
g
Rb (ppm)
Zr (ppm)
h
Rb/Nb (ppm)
Rb (ppm)
Ethiopian Basement
(Peccerillo et al., 1998)
Kone
Fentale
Aluto
Post-caldera mafic (WR)
Post-caldera mafic (glass)
Post-caldera silicic (WR)
Post-caldera silicic (glass)
Caldera (WR)
Caldera (glass)
Pre-caldera (WR)
Pre-caldera (glass)
Kone best fit RhyoliteMELTS model (100MPa, QFM+1, 1wt% H2O)
Fentale best fit RhyoliteMELTS model (100MPa, QFM, 1wt% H2O)
Aluto best fit RhyoliteMELTS model (Gleeson et al., 2017- 100MPa, QFM, 0.5wt% H2O)
Aluto WR range (Hutchison et al., 2016c)

Figure 6.

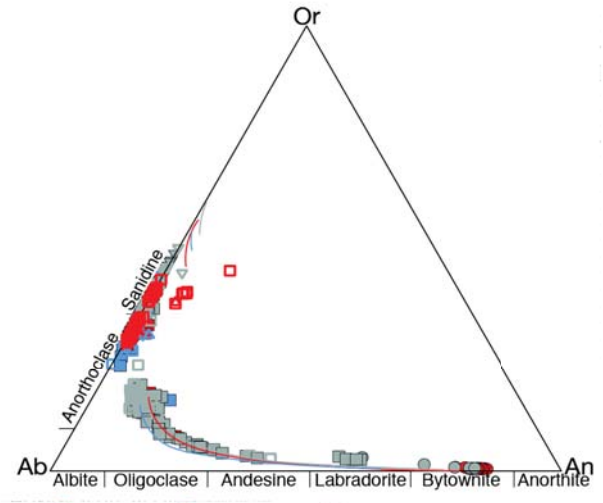

Kone
Fentale
Aluto

Post-caldera silicic (core)
Post-caldera silicic (rim)
Caldera (core)
Caldera (rim)
Pre-caldera (core)
Pre-caldera (rim)

Kone best fit RhyoliteMELTS model (100MPa, QFM+1, 1wt% H_2O)
Fentale best fit RhyoliteMELTS model (100MPa, QFM, 1wt% H_2O)
Aluto best fit RhyoliteMELTS model (Gleeson et al., 2017- 100MPa, QFM, 0.5wt% H_2O)

Figure 7.

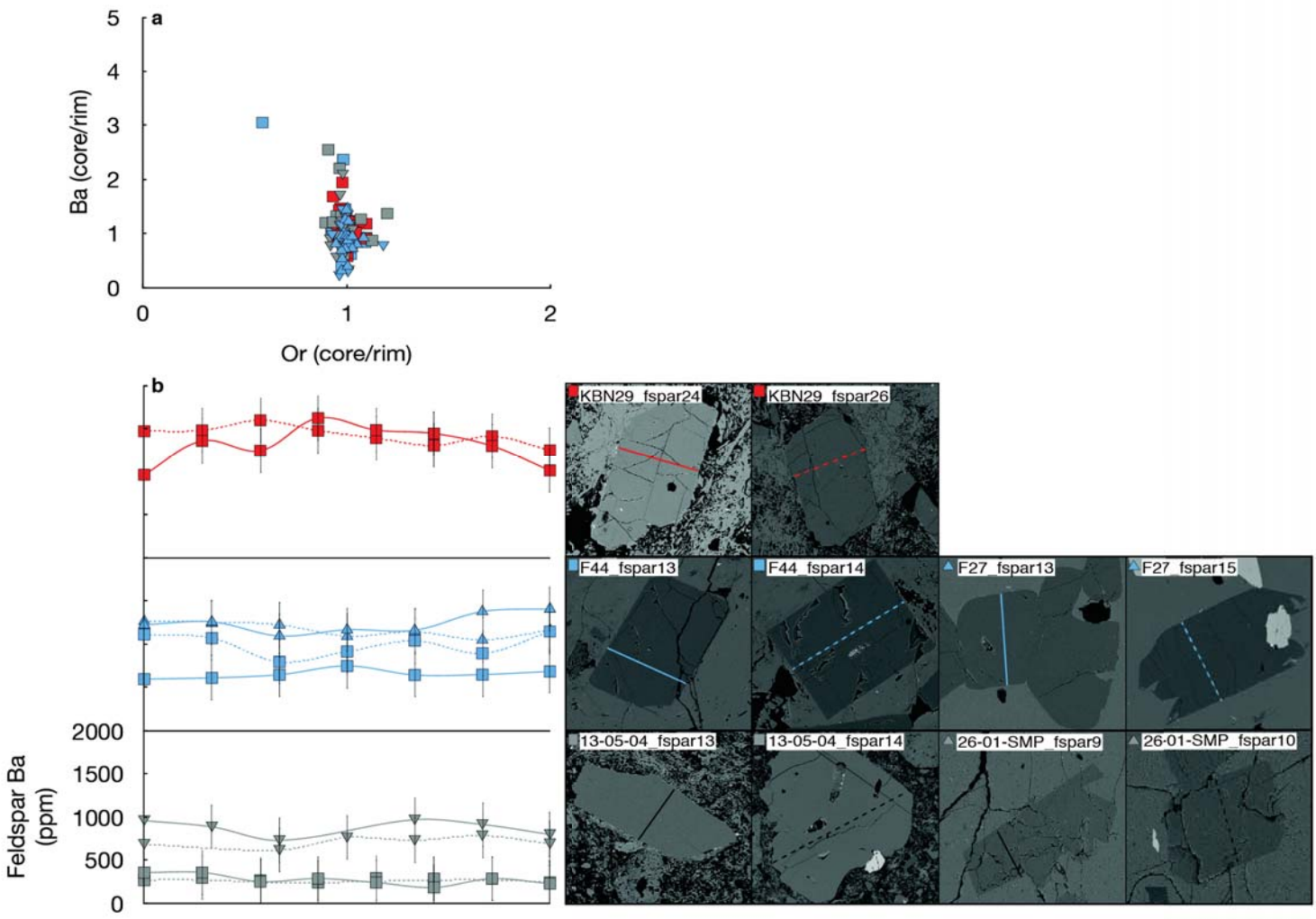
a
Ba (core/rim)
Or (core/rim)
b
Feldspar Ba (ppm)
KBN29_fspar24
KBN29_fspar26
F44_fspar13
F44_fspar14
F27_fspar13
F27_fspar15
13-05-04_fspar13
13-05-04_fspar14
26-01-SMP_fspar9
26-01-SMP_fspar10

Figure 8.

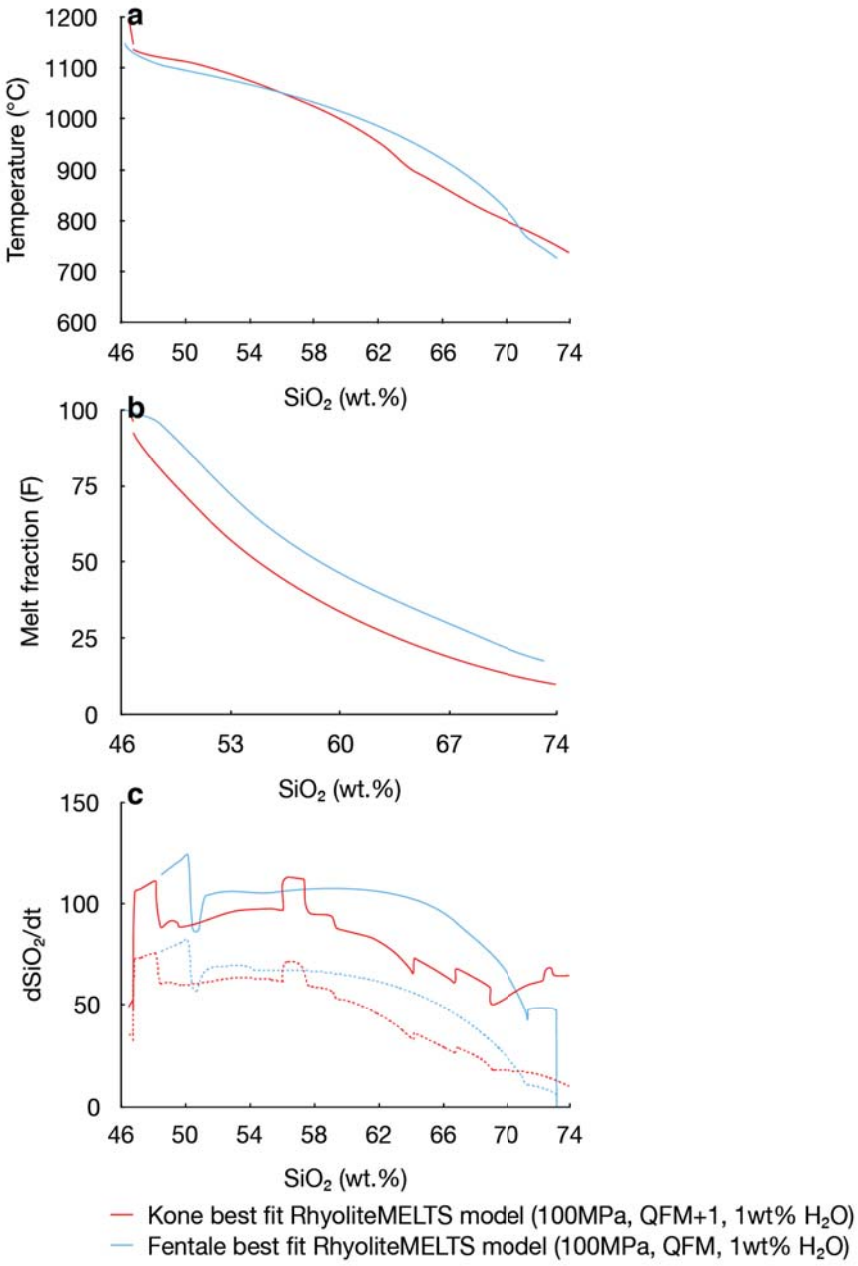
a
Temperature (°C)
1200
1100
1000
900
800
700
600
46
50
54
58
62
66
70
74
SiO2 (wt.%)
b
Melt fraction (F)
100
75
50
25
0
46
53
60
67
74
SiO2 (wt.%)
c
dSiO2/dt
150
100
50
0
46
50
54
58
62
66
70
74
SiO2 (wt.%)
Kone best fit RhyoliteMELTS model (100MPa, QFM+1, 1wt% H2O)
Fentale best fit RhyoliteMELTS model (100MPa, QFM, 1wt% H2O)

Figure 9.

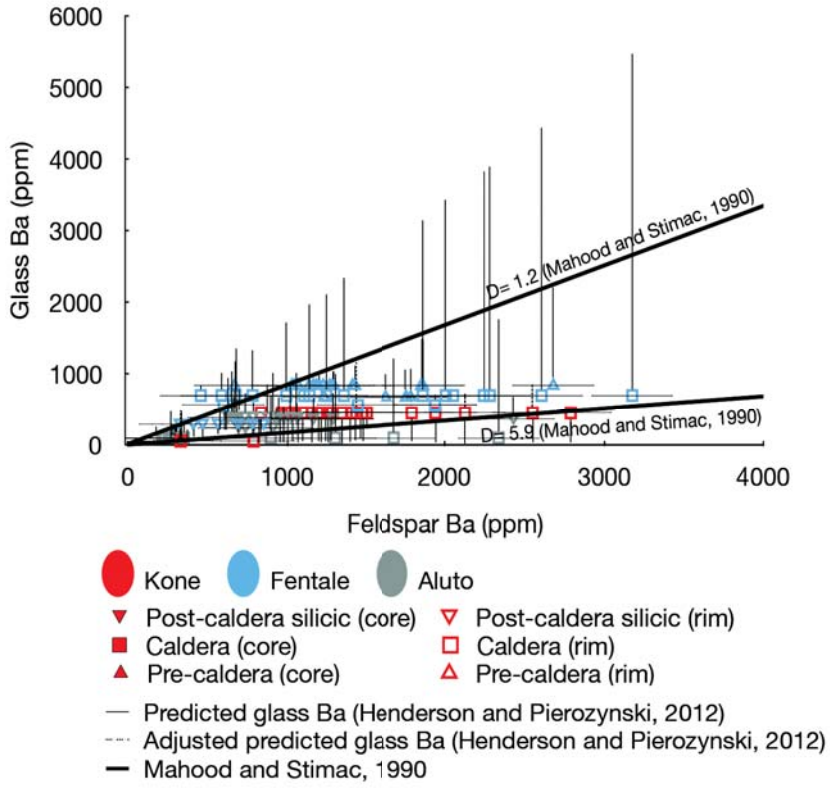
6000
5000
4000
3000
2000
1000
0
Glass Ba (ppm)
0
1000
2000
3000
4000
Feldspar Ba (ppm)
D= 1.2 (Mahood and Stimac, 1990)
D= 5.9 (Mahood and Stimac, 1990)
Kone
Fentale
Aluto
Post-caldera silicic (core)
Post-caldera silicic (rim)
Caldera (core)
Caldera (rim)
Pre-caldera (core)
Pre-caldera (rim)
Predicted glass Ba (Henderson and Pierozynski, 2012)
Adjusted predicted glass Ba (Henderson and Pierozynski, 2012)
Mahood and Stimac, 1990

Figure 10.

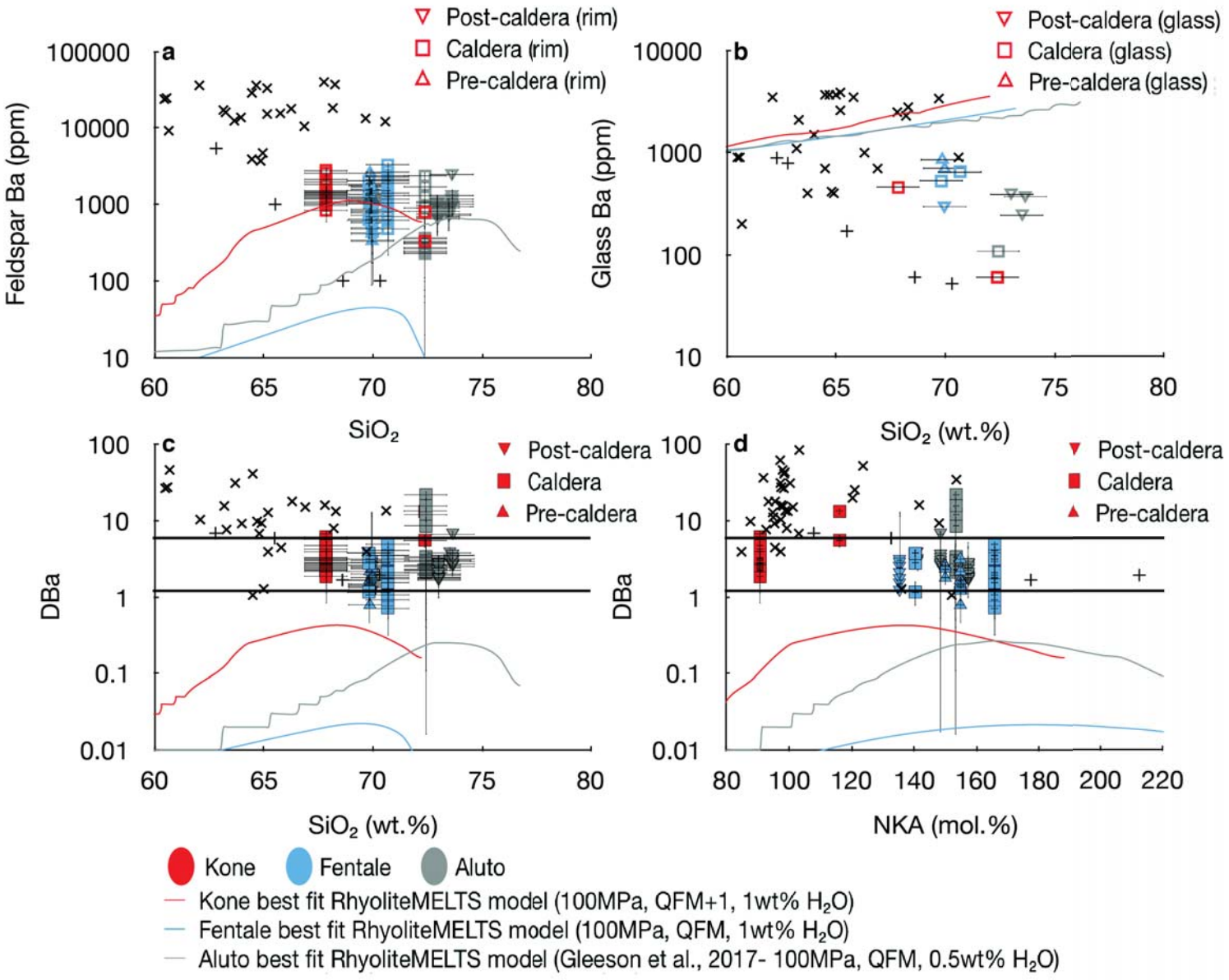
a
Post-caldera (rim)
Caldera (rim)
Pre-caldera (rim)
Feldspar Ba (ppm)
100000
10000
1000
100
10
60
65
70
75
80
SiO2
b
Post-caldera (glass)
Caldera (glass)
Pre-caldera (glass)
Glass Ba (ppm)
10000
1000
100
10
c
Post-caldera
Caldera
Pre-caldera
DBa
100
10
1
0.1
0.01
SiO2 (wt.%)
d
NKA (mol.%)
80
100
120
140
160
180
200
220
Kone
Fentale
Aluto
Kone best fit RhyoliteMELTS model (100MPa, QFM+1, 1wt% H2O)
Fentale best fit RhyoliteMELTS model (100MPa, QFM, 1wt% H2O)
Aluto best fit RhyoliteMELTS model (Gleeson et al., 2017- 100MPa, QFM, 0.5wt% H2O)

Figure 11.

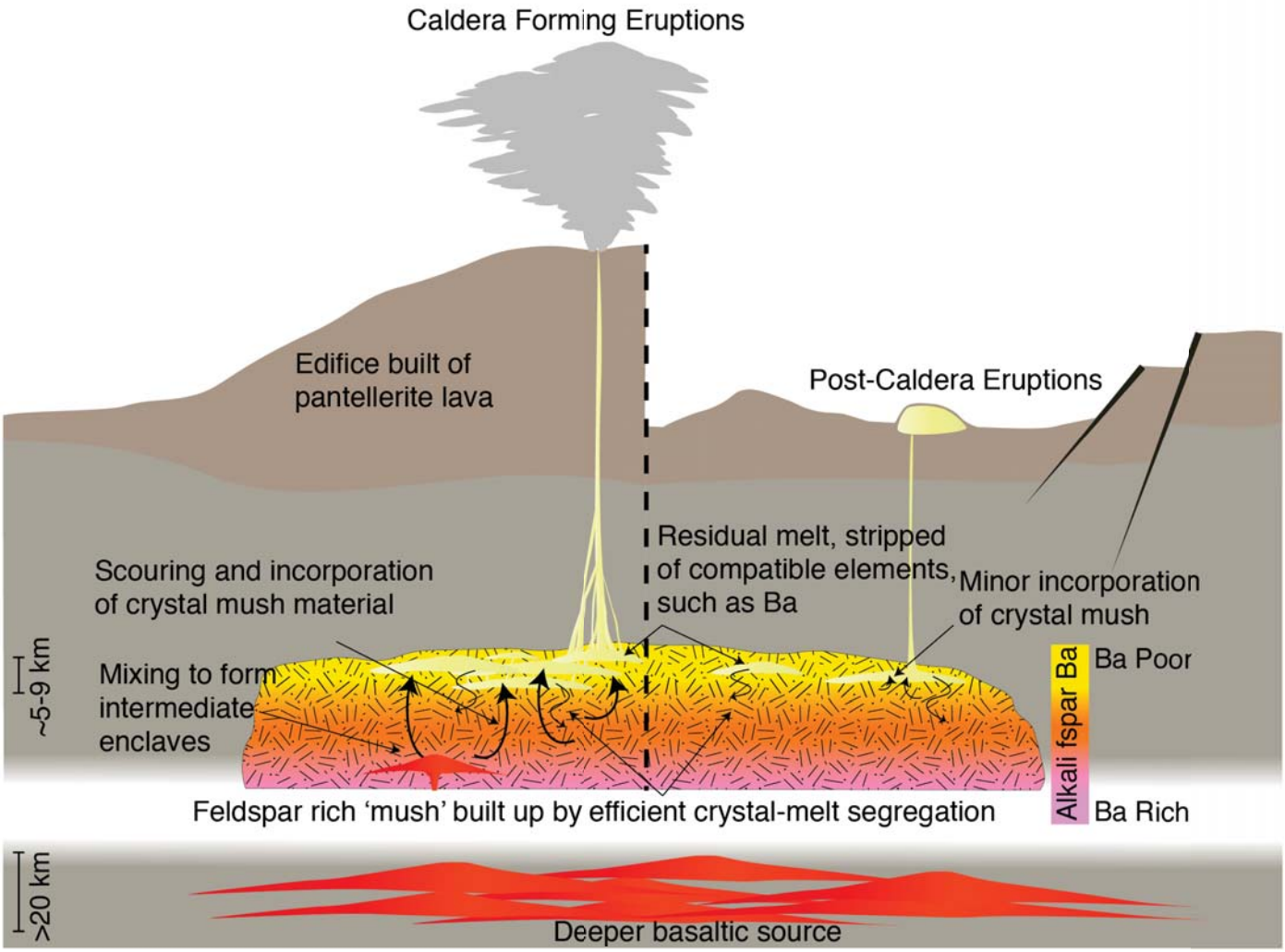
Caldera Forming Eruptions
Edifice built of pantellerite lava
Post-Caldera Eruptions
Residual melt, stripped of compatible elements, such as Ba
Scouring and incorporation of crystal mush material
Minor incorporation of crystal mush
~5-9 km
Mixing to form intermediate enclaves
Ba Poor
Alkali fspar Ba
Ba Rich
Feldspar rich 'mush' built up by efficient crystal-melt segregation
>20 km
Deeper basaltic source

Figure 12.

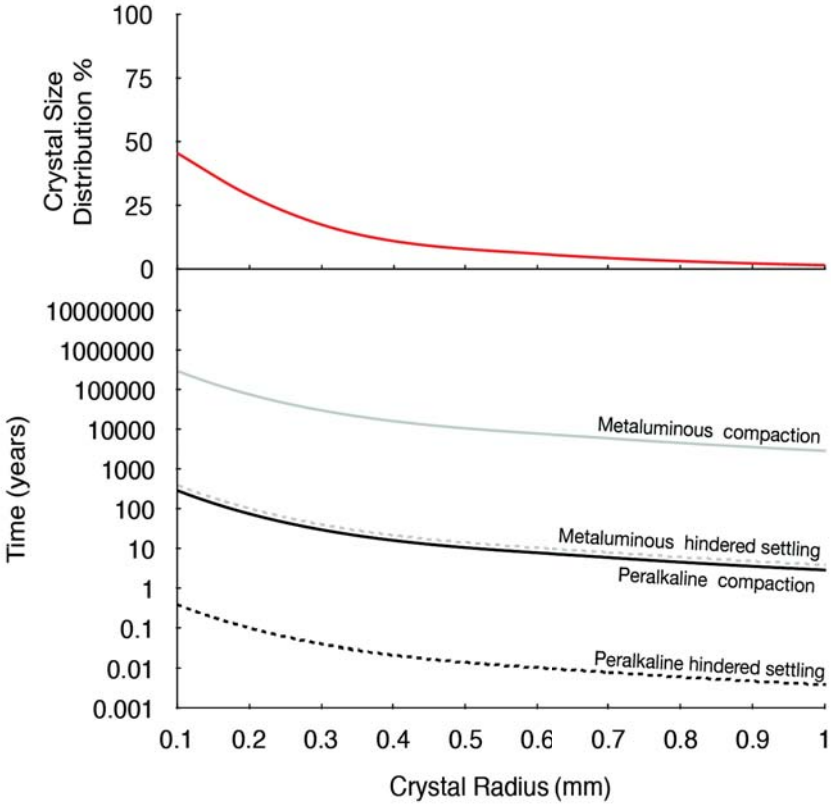
Crystal Size Distribution %
100
75
50
25
0
Time (years)
10000000
1000000
100000
10000
1000
100
10
1
0.1
0.01
0.001
Metaluminous compaction
Metaluminous hindered settling
Peralkaline compaction
Peralkaline hindered settling
0.1
0.2
0.3
0.4
0.5
0.6
0.7
0.8
0.9
1
Crystal Radius (mm)